

# Earth and Space Science



## RESEARCH ARTICLE

10.1029/2023EA003217

### Key Points:

- Bouda is an artisanal and small-scale mining district in Burkina Faso
- Remote sensing using Landsat images allowed us to study the structural control of the expansion of the Bouda site
- Remote sensing using Landsat images allowed to define future exploitation corridors of the Bouda site

### Correspondence to:

R. A. I. Dao,  
dao\_rashid@yahoo.fr

### Citation:

Dao, R. A. I., Ilboudo, H., & Baratoux, D. (2024). Structural controls of the expansion of small-scale artisanal gold of Bouda area (Kaya-Goren Green Belt, Burkina Faso) from remote sensing. *Earth and Space Science*, 11, e2023EA003217. <https://doi.org/10.1029/2023EA003217>



Received 2 AUG 2023

Accepted 16 FEB 2024

### Author Contributions:

**Conceptualization:** R. A. I. Dao  
**Data curation:** R. A. I. Dao  
**Formal analysis:** R. A. I. Dao, H. Ilboudo, D. Baratoux  
**Investigation:** R. A. I. Dao, H. Ilboudo  
**Methodology:** R. A. I. Dao, H. Ilboudo, D. Baratoux  
**Supervision:** H. Ilboudo, D. Baratoux  
**Validation:** R. A. I. Dao, H. Ilboudo, D. Baratoux  
**Visualization:** R. A. I. Dao, H. Ilboudo  
**Writing – original draft:** R. A. I. Dao  
**Writing – review & editing:** H. Ilboudo, D. Baratoux

## Structural Controls of the Expansion of Small-Scale Artisanal Gold of Bouda Area (Kaya-Goren Green Belt, Burkina Faso) From Remote Sensing

R. A. I. Dao<sup>1</sup> , H. Ilboudo<sup>1</sup>, and D. Baratoux<sup>2,3</sup> 

<sup>1</sup>Laboratoire Géosciences et Environnement, UFR en Sciences de la Vie et de la Terre, Université Joseph KI-ZERBO, Ouagadougou, Burkina Faso, <sup>2</sup>Géosciences Environnement Toulouse, Université de Toulouse, CNRS & IRD, Toulouse, France, <sup>3</sup>UFR des Sciences de la Terre et des Ressources Minières, Université Félix Houphouët-Boigny, Abidjan, Côte d'Ivoire

**Abstract** Small-scale artisanal mining is a vital sector of the economy of Burkina Faso. This activity, correctly regulated, remains essential for the population despite security issues since 2015. Exploration of new areas for gold mining in this condition is difficult but essential to continue extractive activities. It is, therefore, important to define viable corridors, with science-based evidence for the good prospects, to support artisanal miners' activities in a way that minimizes the environmental impact. We describe a remote sensing approach to study the structural control of expanding small-scale artisanal gold activity at the Bouda site and define future mining corridors. This remote sensing approach can also mitigate and remedy environmental impacts. The Minimum Noise Fraction (MNF) is applied to Landsat images (7-ETM+, 5-TM, and 8-OLI, respectively, for 2000, 2011, and 2022) to detect extraction sites and perform a spatiotemporal analysis of the expansion of areas affected by gold extraction. The near-infrared and mid-infrared bands of Landsat images significantly contribute to detecting extraction areas. A morphological study of the site over time and Principal Component Analysis (PCA) on Landsat 8-OLI enable us to perform a lineament analysis. The expansion of mining activity is structurally controlled, as revealed by the correlation between gold occurrences and high lineament densities, especially in the dominant NE-SW direction. These analyses suggest five potential prospecting corridors in the Bouda site.

## 1. Introduction

Artisanal mining was once considered an activity practiced by farmers and poor populations to meet their daily needs due to the declining productivity of their crops caused by the dry season and/or climate change. Today, this activity is Africa's most important rural non-agricultural activity (Abass Saley et al., 2021; Hilson, 2020; Ngom, Baratoux, et al., 2022). In Burkina Faso, artisanal and small-scale mining (ASM) is legally practiced under an Authorization of Artisanal Exploitation (AEA, standing for Autorisation d'Exploitation Artisanale, in French). The DGMG (General Department of Mines and Geology) grants the AEA. Without AEA, artisanal mining is illegal.

The Bouda site, located in northern Burkina Faso, within the Passoré province, specifically near the Pélegtenga village (see Figures 1 and 2), is legally exploited and well organized. A farmer discovered the site by chance at the end of 1987, and mining began in January 1988 (Nana, 1992). The mineralization is structurally controlled. This activity provided economic benefits to the population. Unfortunately, the country has been plagued by terrorist attacks since 2015, causing massive population displacements estimated at nearly 1.5 million people by 2022 (OCHA, 2022).

The Bouda site, among other sites, is still active, showing the vital capacity and resilience of the population, able to maintain the activity despite the lack of security. However, this situation slows down geological exploration and the possibility of discovering new prospects. It is, therefore, necessary to find alternative techniques to continue geological exploration and monitor the expansion, evolution, and abandonment of artisanal mining sites. Remote sensing offers a promising alternative when field investigations must be limited. Remote sensing has been successfully used in exploration geology (Bedini, 2011, 2017; Hu et al., 2018; Ibrahima et al., 2018; Pour & Hashim, 2015a, 2015b) for interpreting spectral signatures over relatively large areas of interest (Girija & Mayappan, 2019; Rajesh, 2004) and identifying new prospects (Amer et al., 2012; Pour & Hashim, 2011). These

© 2024 The Authors. Earth and Space Science published by Wiley Periodicals LLC on behalf of American Geophysical Union.

This is an open access article under the terms of the [Creative Commons Attribution-NonCommercial-NoDerivs License](https://creativecommons.org/licenses/by/4.0/), which permits use and distribution in any medium, provided the original work is properly cited, the use is non-commercial and no modifications or adaptations are made.

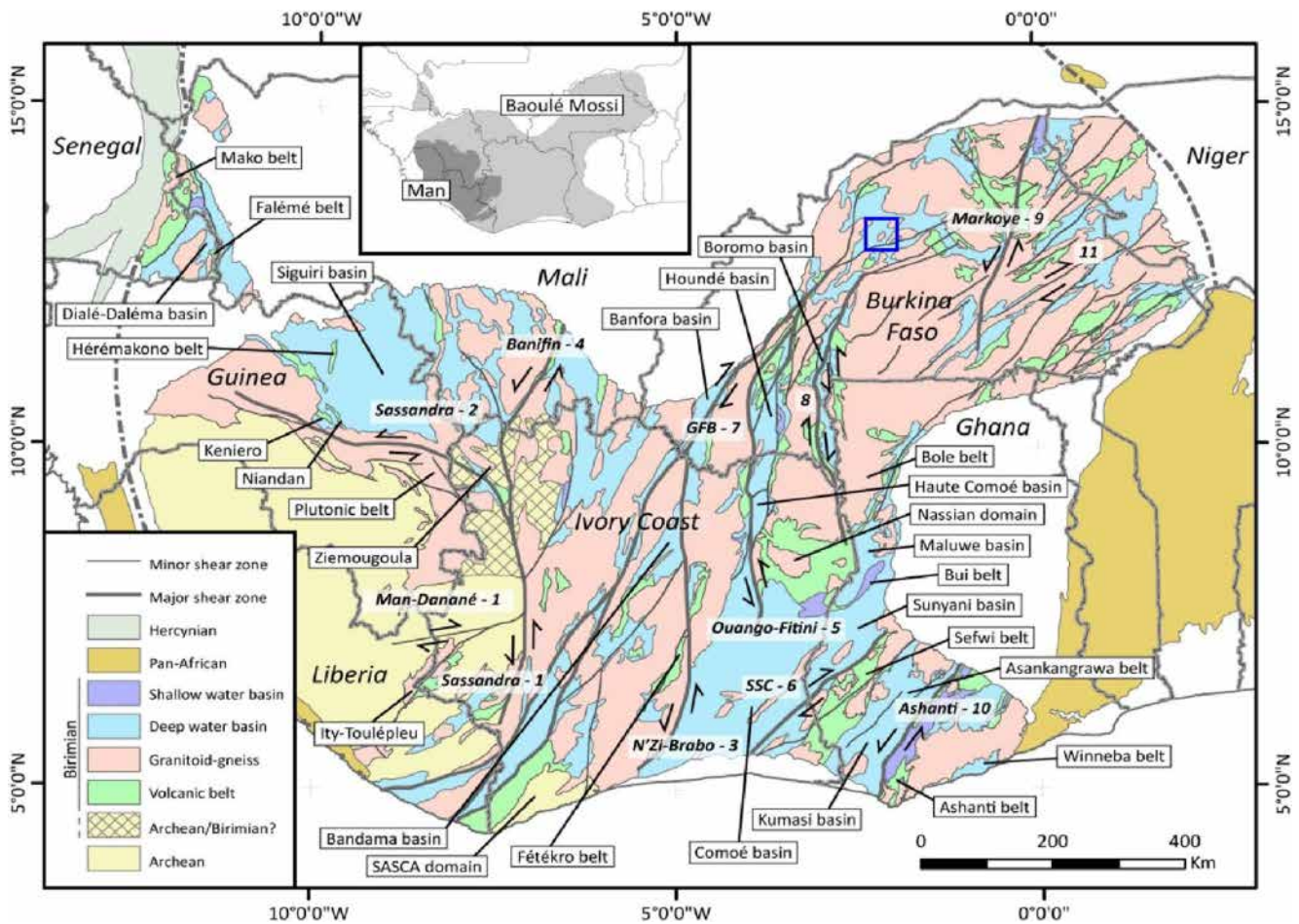


**Figure 1.** Synthetic geologic map of the Leo Ridge (modified after Grenholm (2014)) showing the study area with a blue frame.

tools were also successfully employed for mapping and monitoring the expansion and environmental impacts of artisanal mining in Ghana (Forkuor et al., 2020), Senegal (Ngom et al., 2020), Côte d'Ivoire (Ngom, Mbaye, et al., 2022), Niger (Abass Saley et al., 2021). The current study aims to optimize the definition of prospecting corridors in the Bouda area based on the spatiotemporal dynamics of exploitation correlated with structural analysis. The remote sensing-assisted definition of prospecting corridors shall potentially help artisanal miners exploring new places and ensure the sustainability of their activity.

## 2. Regional and Local Geology

The Bouda site (Burkina Faso) and its mineralization occur in the southern part of the West-African Craton (WAC), which is divided into the Paleoproterozoic (Birimian) Baoulé-Mossi domain in the east and the Archean Kénéma-Man domain in the west (Grenholm et al., 2019; Masurel et al., 2022; Figure 1). The Bouda site is located in the Baoulé-Mossi domain, comprised of granites and greenstone belts (Baratoux et al., 2011; Hirdes et al., 1996; Milési et al., 1992). These Paleoproterozoic rocks are exposed over approximately 80% of the surface area of Burkina Faso. Still, they are covered on the country's western, northern, and eastern margins by Neoproterozoic to Cambro-Ordovician formations of sedimentary rocks (1,000–435 Ma). The geodynamic setting is still debated and implies either oceanic plateaus related to a mantle plume (Augustin & Gaboury, 2017; Baratoux et al., 2011) or volcanic island arcs (Baratoux et al., 2011; de Kock et al., 2012; Ganne et al., 2012; Ilboudo et al., 2020). The belts are essentially made up of metavolcanic rocks, ranging from metabasalts to metarhyolites and metasedimentary rocks, including quartzites and metapelites (Baratoux et al., 2011; Ilboudo et al., 2017, 2020). The greenstone belts are the most prolific for gold and base metals, which are mainly structurally

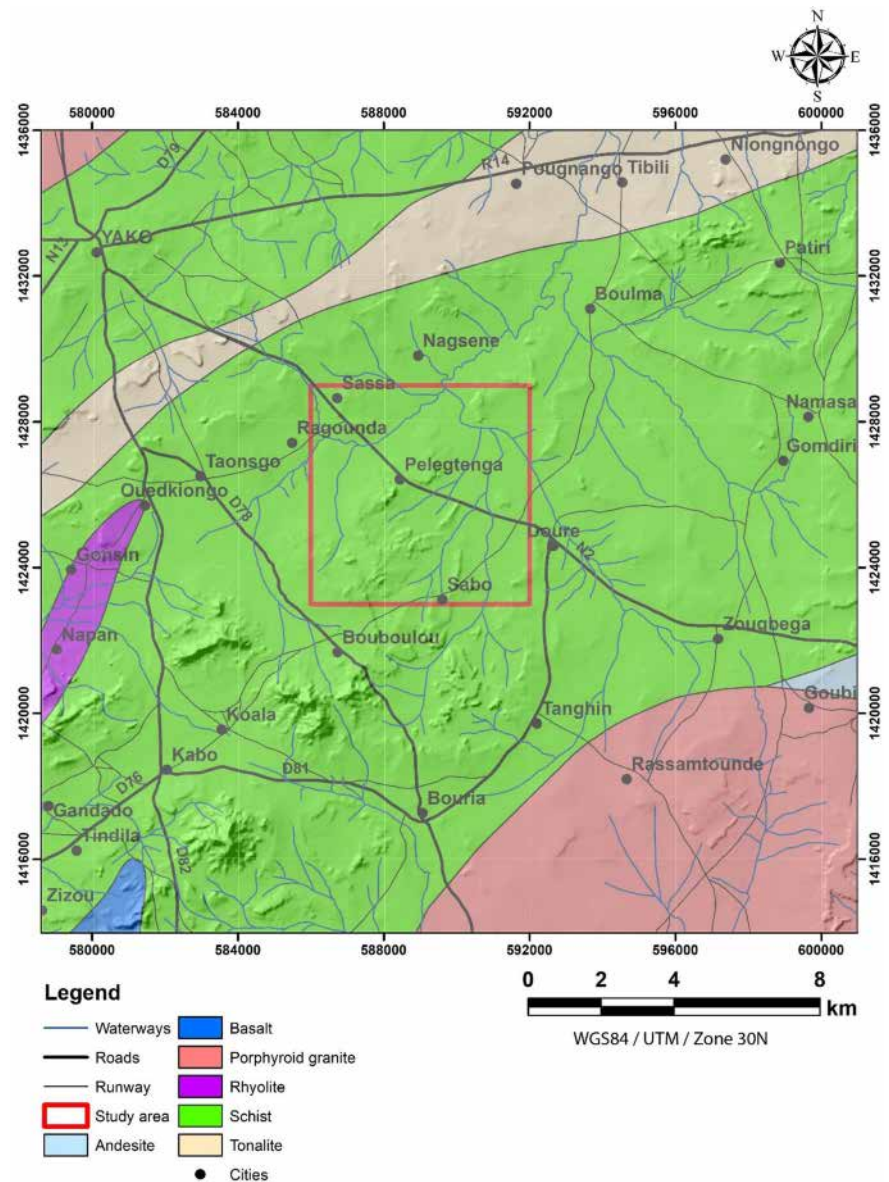


**Figure 2.** Study area showing the Bouda site (red frame) on a 1:200,000 geologic map from Chevremont et al. (2003), Projection WGS84/UTM Zone 30N. Shaded relief in the background has been calculated from SRTM Data.

controlled (Augustin & Gaboury, 2017; Baratoux et al., 2011; Goldfarb et al., 2017; Markwitz et al., 2016; Masurel et al., 2022).

The Bouda site (Figure 2) is located in a NE-SW flexure of the Boromo-Goren greenstone belt (Figures 1 and 2), where the rocks consist of conformable successions of meta-sedimentary rocks that are intercalated with volcanic rocks. These successions are intercalated with a suite of intermediate mafic volcanic rocks, volcanic breccias, and tuffs (Hein et al., 2004). This assemblage was intruded by granites. The belt hosts several world-class metal deposits, notably Poura, Bissa Gold, and Perkoa (Aziz et al., 2016; Markwitz et al., 2016).

Preliminary fieldwork conducted on the Bouda site shows that it comprises doleritic basalts (Figure 3a), gabbros (Figure 3b), and metamorphic rocks composed of metabasalts (Figure 3c) and metapelites (Figure 3d) that host the mineralized and gold-bearing quartz vein.

Regolith is not abundant and is discontinuous in the study area but is present in an open pit. At this location, its depth is 2 m (to the base of the saprock) and is marked by kaolinitic and hematitic alteration.



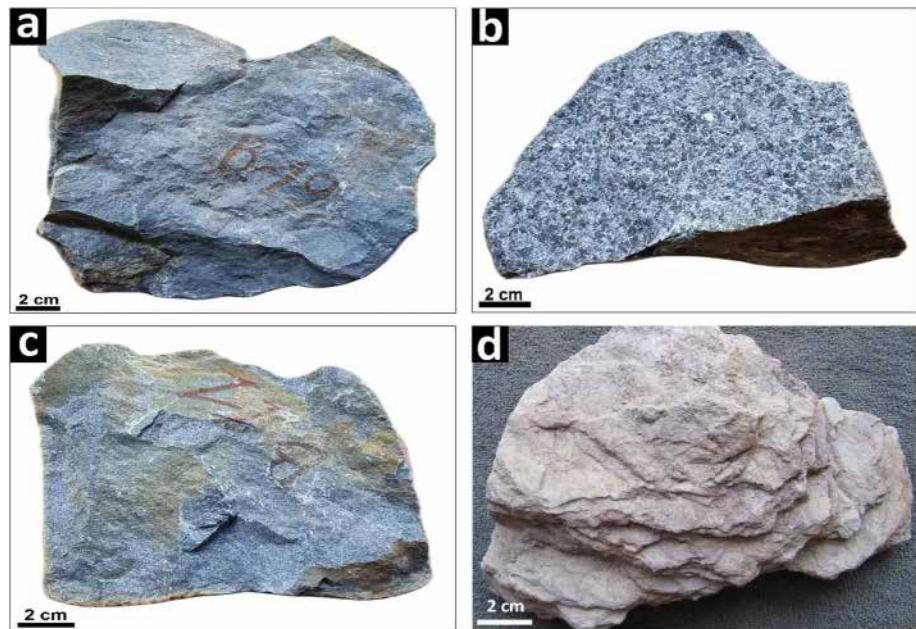


**Figure 3.** Dominant rock types present in the Bouda area. (a) Doleritic basalt; (b) Gabbro; (c) Metabasalt; (d) Metapelite.

### 3. Materials and Methods

Our approach is based on standard remote sensing techniques applied on Landsat imagery. The Minimum Noise Fraction (MNF) and Principal Component Analysis (PCA) followed by direction filters were applied as alternative approaches to identify potential mining sites (Figure 4). The two techniques have been successfully used for the detection of mining sites in other locations (Abass Saley et al., 2021; Aretouyap et al., 2020; Gannouni & Gabtni, 2015; Ghislain et al., 2021; Ibrahim & Mutua, 2014; Ourhzif et al., 2019). Due to insecurity issues, a short period of fieldwork (3 days) was carried out on the Bouda site. It consisted of recording the coordinates of some extraction areas (considered to be gold-bearing areas), dwellings, and bare ground. They are named “ground checkpoints.”

#### 3.1. Data Acquisition and Pre-Processing

##### 3.1.1. Data Acquisition and Fieldwork

Satellite images used for the study consist of Landsat 5-TM, 7-ETM+, and 8-OLI images. Landsat 7-ETM+ images were considered for the year 2000, Landsat 5-TM images for 2011, and Landsat 8-OLI images for 2022. It is important to note that since June 2003, the Landsat 7-ETM+ satellite sensor has been acquiring and delivering data with gaps caused by the failure of the scan line corrector (SLC). Table 1 explains the characteristics of each type of image used. These images are in the public domain and were downloaded from [www.earthexplorer.usgs.gov](http://www.earthexplorer.usgs.gov). Three scenes spanning two decades (2000, 2011, 2022) were selected with the following criteria: images acquired during the dry season from February to April and with cloudiness cover less than 5%. This temporal frequency (one scene per decade) was chosen in adequation with the spatial dynamics of the site, previously noted using Google Earth Pro 7.3 archive images.

The goal of the fieldwork was to record the coordinates of extraction areas, bare ground, and dwellings. These ground checkpoints were chosen to perform the spectral analysis of the satellite images and validate the interpretations.

##### 3.1.2. Pre-Processing of Satellite Images

Optical remote sensing images commonly contain radiometric and geometric errors due to the combined effects of the atmosphere, instruments used, sunlight, and topography (Dubois, 1999; Richards & Jia, 2006). These errors manifest in various types of noise in remotely sensed images, which must be minimized to reduce their impact on

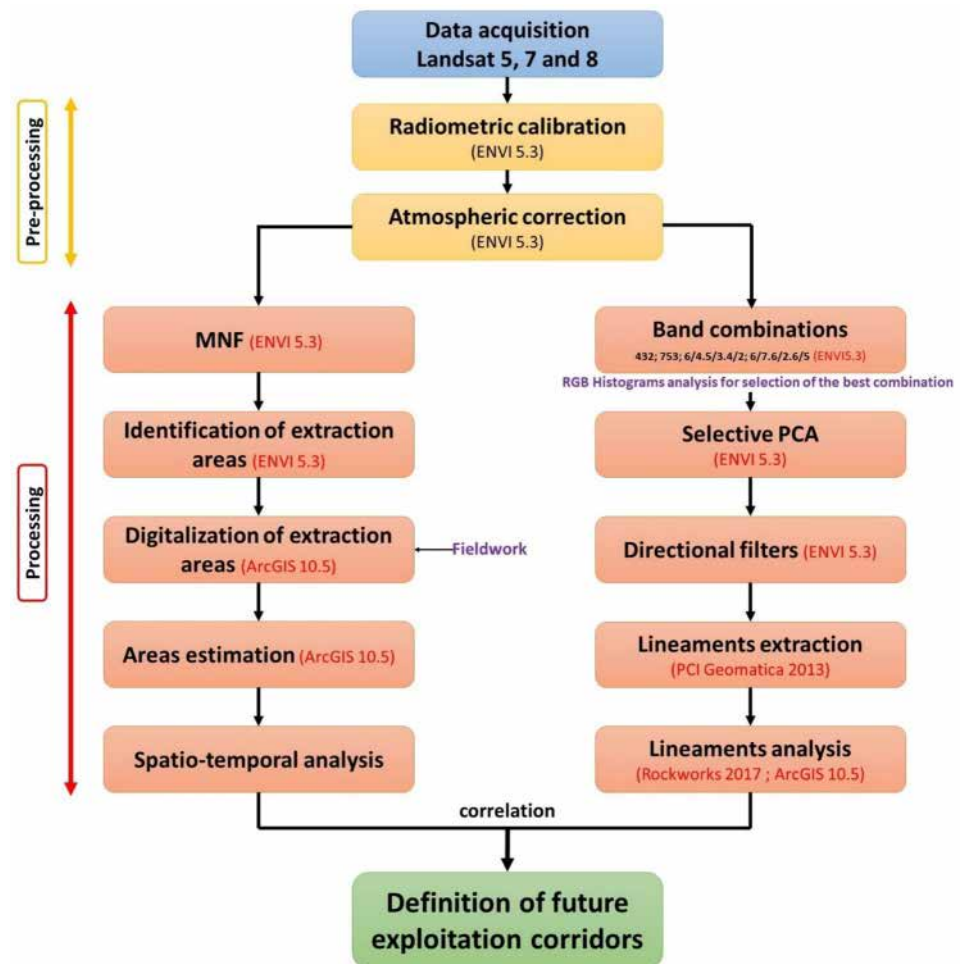


**Figure 4.** Flowchart showing the main steps of our methodology.

the mapping products derived from these images. The Landsat imagery used in this work has a level 1 accuracy and terrain correction (level 1T). They are orthorectified using ground checkpoints and elevation data provided by a digital elevation model (DEM). The pre-processing of the Landsat data includes radiometric calibration and atmospheric correction using the Fast Line of Sight Atmospheric Analysis of Spectral Hypercubes (FLAASH) module of ENVI 5.3 software (Javhar et al., 2019; Wambo et al., 2020).

### 3.2. Spatiotemporal Analysis Method

The application of Minimum Noise Fraction (MNF) is used for the identification of the extraction areas (Figure 4, left branch) following a previously successful application in the Sahelian region (Abass Saley et al., 2021). Fieldwork data were examined in Google Earth Pro 7.3 software (archive images) and used to refine the contours of extraction areas with greater precision. Figure 5 shows an example of the spectral signature of extraction zones in MNF and Google Earth Pro 7.3. ArcGIS 10.5 software was used to digitize the polygons of extraction areas to estimate their surface areas. MNF output overlaid on Google Earth Pro 7.3 archive images was used for this purpose.

The MNF algorithm consists of two successive principal component (PC) transforms (Green et al., 1988). The first PC transform focuses on noise whitening by decorrelating and scaling the noise in the data, producing data with a variance of one (1) and no inter-band correlation (Shawky et al., 2019). This transformed data was subjected to a second standard PC transform, resulting in a final uncorrelated output organized according to information content reduction (Research Systems, Inc, 2003).

**Table 1**  
*Spectral and Spatial Characteristics of Landsat-5 TM, Landsat-7 ETM+, and Landsat 8-OLI Data*

|                | Spectral bands              | Wavelengths ( $\mu\text{m}$ ) | Spatial resolution (m) | Acquisition date and time                           |
|----------------|-----------------------------|-------------------------------|------------------------|---|
| Landsat 5-TM   | <b>Band 1</b> —Blue         | 0.45–0.52                     | 30                     | 08 February 2011 at 10hr 16 min 01 s Cloud cover: 0 |
|                | <b>Band 2</b> —Green        | 0.52–0.60                     | 30                     |   |
|                | <b>Band 3</b> —Red          | 0.63–0.69                     | 30                     |   |
|                | <b>Band 4</b> —NIR          | 0.76–0.90                     | 30                     |   |
|                | <b>Band 5</b> —SWIR 1       | 1.55–1.75                     | 30                     |   |
|                | <b>Band 6</b> —TIR          | 10.40–12.50                   | 120                    |   |
|                | <b>Band 7</b> —SWIR 2       | 2.08–2.35                     | 30                     |   |
| Landsat 7-ETM+ | <b>Band 1</b> —Blue         | 0.441–0.514                   | 30                     | 18 February 2000 at 10hr 18 min 44 s Cloud cover: 0 |
|                | <b>Band 2</b> —Green        | 0.519–0.601                   | 30                     |   |
|                | <b>Band 3</b> —Red          | 0.631–0.692                   | 30                     |   |
|                | <b>Band 4</b> —NIR          | 0.772–0.898                   | 30                     |   |
|                | <b>Band 5</b> —SWIR 1       | 1.547–1.749                   | 30                     |   |
|                | <b>Band 6</b> —TIR          | 10.31–12.36                   | 60                     |   |
|                | <b>Band 7</b> —SWIR 2       | 2.064–2.345                   | 30                     |   |
|                | <b>Band 8</b> —Panchromatic | 0.515–0.896                   | 15                     |   |
| Landsat 8-OLI  | <b>Band 1</b> —Aerosol      | 0.433–0.453                   | 30                     | 27 April 2022 at 10hr 25 min 49 s Cloud cover: 0.03 |
|                | <b>Band 2</b> —Blue         | 0.450–0.515                   | 30                     |   |
|                | <b>Band 3</b> —Green        | 0.525–0.600                   | 30                     |   |
|                | <b>Band 4</b> —Red          | 0.630–0.680                   | 30                     |   |
|                | <b>Band 5</b> —NIR          | 0.845–0.885                   | 30                     |   |
|                | <b>Band 6</b> —SWIR 1       | 1.560–1.660                   | 30                     |   |
|                | <b>Band 7</b> —SWIR 2       | 2.100–2.300                   | 30                     |   |
|                | <b>Band 8</b> —Panchromatic | 0.500–0.680                   | 15                     |   |
|                | <b>Band 9</b> —Cirrus       | 1.360–1.390                   | 30                     |   |

Note. NIR = Near Infrared, SWIR = shortwave infrared, TIR: Thermal Infrared.

### 3.3. Lineaments Analysis Method

The lineament analysis (Figure 4, right branch) was completed utilizing only the Landsat 8-OLI satellite image (the most recent one having the highest resolution). During our fieldwork, we noticed that mineral exploitation was done in a preferential direction and that extraction sites are elongated in a single direction. This was confirmed by plotting the points and analyzing the images on Google Earth Pro 7.3. We, therefore, chose to study the structural control of the mining exploitation by extracting the lineaments of the site by remote sensing to see possible correlations between structural elements and the direction of expansion of the mining sites. To this end, to highlight the lineaments related to tectonism, we first applied combinations and ratios of spectral bands to determine the best combination to delineate lithological contacts by analyzing histograms of RGB bands. We then used a selective Principal Component Analysis (PCA) on the best combination determined in the previous step, followed by directional filters to decorrelate the spectral bands and extract the lineaments. The details of each step are presented in the next paragraph.

#### 3.3.1. Combinations and Ratios of Bands

Band combinations and ratios are commonly used enhancement techniques on multispectral optical remote sensing images for discriminating between different rock units (Rezaei et al., 2020). Spectral band ratios reduce topography effects in remote sensing images and enhance specific features related to the reflectance spectrum of target rocks (Richards & Jia, 2006). The combinations and band ratios applied here are derived from Abdessamad et al. (2018), who synthesized the different band combinations and band ratios in the Landsat image processing chain for lithology discrimination. As a result, the **4.3.2** and **7.5.3** RGB mode combinations and the **6/4.5/3.4/2**

and 6/7.6/2.6/5 band ratio RGB mode combinations were applied, where numbers represent Landsat 8-OLI channels as given in Table 1. The best combination for unit discrimination was chosen based on band histogram analysis. Experimental lithological limits were drawn on the best image and overlaid on the other combinations for better visualization of the boundaries between each unit.

### 3.3.2. Selective Principal Component Analysis (PCA)

Satellite imagery consists of interdependent multispectral bands that contain redundant information. This property can be used to reduce the dimension of the data and produce data sets that are easier to analyze and visualize, with much of the information (variance) preserved. The PCA technique is an effective statistical technique for this purpose. By removing redundant data and isolating noise or topography, the relevant spectral information is concentrated and preserved in a small number of uncorrelated bands called principal components (Adiri et al., 2016; Han et al., 2018; Liu & Philippa Mason, 2009; Loughlin, 1991; Sheikhrhimi et al., 2019). This type of processing is based on linear algebraic raster operations and multivariate statistics and provides an efficient method for lineament detection (Li et al., 2010). Each principal component output contains data from different input bands (Adiri et al., 2020), and each band contribution can be determined by examining the eigenvectors. A selective PCA is applied to the band combination determined in the previous step to concentrate the maximum spectral information related to lithologies in the first principal component before applying the direction filters to extract the lineaments.

### 3.3.3. Directional Filters

Lineaments are represented as textural discontinuities, such as the edges of relatively uniform regions associated with high frequencies or strong reflectance transitions. The geometric edge enhancement and detection method is based on convolutional filtering (Moore & Waltz, 1983). Consecutive elements of the original image are multiplied by the convolution window values, and the results are combined to form the resulting image. The first band of the PCA output applied to either the combinations of bands or band ratios (depending on which one best discriminates the lithologies) is used for enhancement and edge detection. Directional filtering using gradient enhancement matrices of different sizes is widely used for lineament extraction from Landsat 8-OLI images (Aretouyap et al., 2020; Gannouni & Gabtni, 2015; Ibrahim & Mutua, 2014; Mwaniki et al., 2015; Suzen & Toprak, 1998). As the matrix size increases, the number of affected pixels increases and the gradient map becomes more blurred (Aretouyap et al., 2020). Considering the Landsat resolutions of 30 m per pixel and the typical sizes of lineaments of interest (fault zones), a  $3 \times 3$  matrix is the most appropriate. Also, directional filters were applied in N-S, NE-SW, E-W, and NW-SE directions to search for the different orientations of lineaments.

### 3.3.4. Extraction of the Lineaments

In the gradient images resulting from applying the directional filters, the lineaments appear as linear features associated with abrupt changes in the neighboring pixels corresponding to high absolute gradient values. Automatic extraction of lineaments from the gradient image was performed using PCI Geomatica 2013 software with the “Line Extraction” module. The first principal component (PC1) was processed with the parameters listed in Table 2 that are optimal for detecting tectonic related lineaments (Endyana et al., 2018). The reader is referred to [https://catalyst.earth/catalyst-system-files/help/references/pciFunction\\_r/easi/E\\_line.html](https://catalyst.earth/catalyst-system-files/help/references/pciFunction_r/easi/E_line.html) for the definition of each of these parameters. The data for roads and tracks from the National Topographic Database provided by the Geographic Institute of Burkina Faso (IGB) were used to eliminate bias in the lineaments detection. These data are available upon request from the Institute. Thus, the lineaments related to roads and tracks were removed. Also, only the automatically detected lineament is retained for duplicate detections of lineaments that appear in the images associated with different filter directions. Finally, three lineaments were identified and manually traced during a manual check. The RockWorks 2017 and ArcGIS 10.5 software packages were then used to analyze extracted lineaments’ distribution, orientation, and length. The lineament distribution analysis was supported by a lineament density map expressed as a percentage of lineaments per unit area.



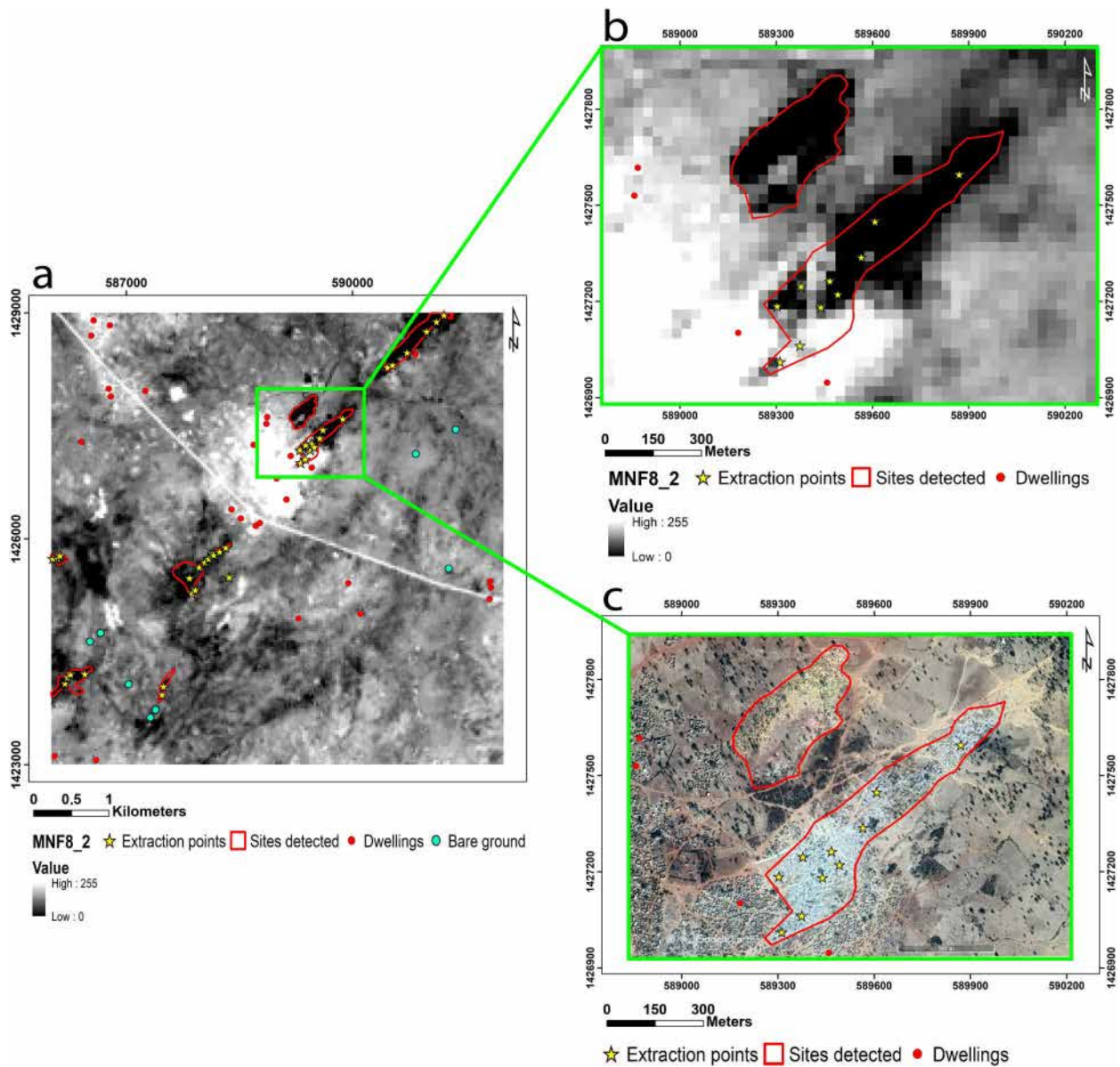


**Figure 5.** Example of site detection on the MNF output and Google Earth (Projection WGS84/UTM Zone 30N): (a) Sites detected on MNF output; (b) Zoomed image of an extraction site seen on the MNF image; (c) Contour refinement with Google Earth.

**Table 2**

Parameters Used to Extract Lineaments in the PCI Geomatica 2013 Software Automatically

| Parameters                         | Used values |
|------------------------------------|-------------|
| RADI: filter radius                | 5           |
| GTHR: Edge Gradient Threshold      | 75          |
| LTHR: Curve Length Threshold       | 2           |
| FTHR: Line Fitting Threshold       | 10          |
| ATHR: Angular Difference Threshold | 20          |
| DTHR: Linking Distance Threshold   | 1           |

## 4. Results

### 4.1. Results of the Spatiotemporal Analysis

#### 4.1.1. Identification of Extraction Sites (MNF Application)

- Landsat 7-ETM+ (year 2000)

Table 3 shows the eigenvectors matrix from the MNF application on the Landsat 7-ETM+ image, whereas Figure 6 presents the MNF images. Ore extraction activity began in the areas highlighted by yellow frames marked on the MNF images (Figure 6). MNF7-1 concentrates the maximum information (45.85%), followed by MNF7-2 (17.51%) and MNF7-3 (15.53%) (total: 79.89%). The remaining MNFs (MNF7-4, MNF7-5, and MNF7-6) contain



**Table 3**  
MNF Band Eigenvector Matrix From Landsat-7 ETM+

| Eigenvectors | Band 1 | Band 2 | Band 3 | Band 4 | Band 5 | Band 6 | Eigenvalues (%) |
|--------------|--------|--------|--------|--------|--------|--------|-----------------|
| MNF7-1       | -0.551 | -0.622 | 0.192  | -0.508 | 0.111  | -0.008 | 45.85           |
| MNF7-2       | -0.433 | -0.336 | -0.121 | 0.826  | -0.039 | 0.025  | 17.51           |
| MNF7-3       | 0.569  | -0.473 | 0.640  | 0.197  | -0.040 | 0.0004 | 15.53           |
| MNF7-4       | -0.278 | 0.413  | 0.547  | 0.139  | 0.601  | -0.266 | 9.73            |
| MNF7-5       | -0.324 | 0.307  | 0.471  | -0.013 | -0.757 | 0.068  | 8.14            |
| MNF7-6       | -0.047 | 0.096  | 0.122  | 0.012  | 0.222  | 0.961  | 3.20            |

less spectral information (Figures 6d–6f), with 9.73%, 8.14%, and 3.20% of eigenvalues for MNF7-4, MNF7-5, and MNF7-6, respectively. MNF7-1 cannot discriminate between extraction areas, dwellings, and bare ground, as MNF-1 pixel values are randomly distributed for each terrain type. MNF7-2 highlights extraction areas in white pixels, but there is a lack of discrimination between extraction areas and dwellings; bare ground is shown in white and gray. The control points pixel values for MNF7-3 and MNF7-4 are randomly distributed; therefore, the two bands are useless for discriminating the land use. Extraction areas stand out on MNF7-5 as bright pixels (high pixel values). MNF7-6, on the other hand, is very noisy. MNF7-5 was then used to identify the mining site and the extent of the activity for 2000, aided by verifications and refinement in Google Earth imagery.

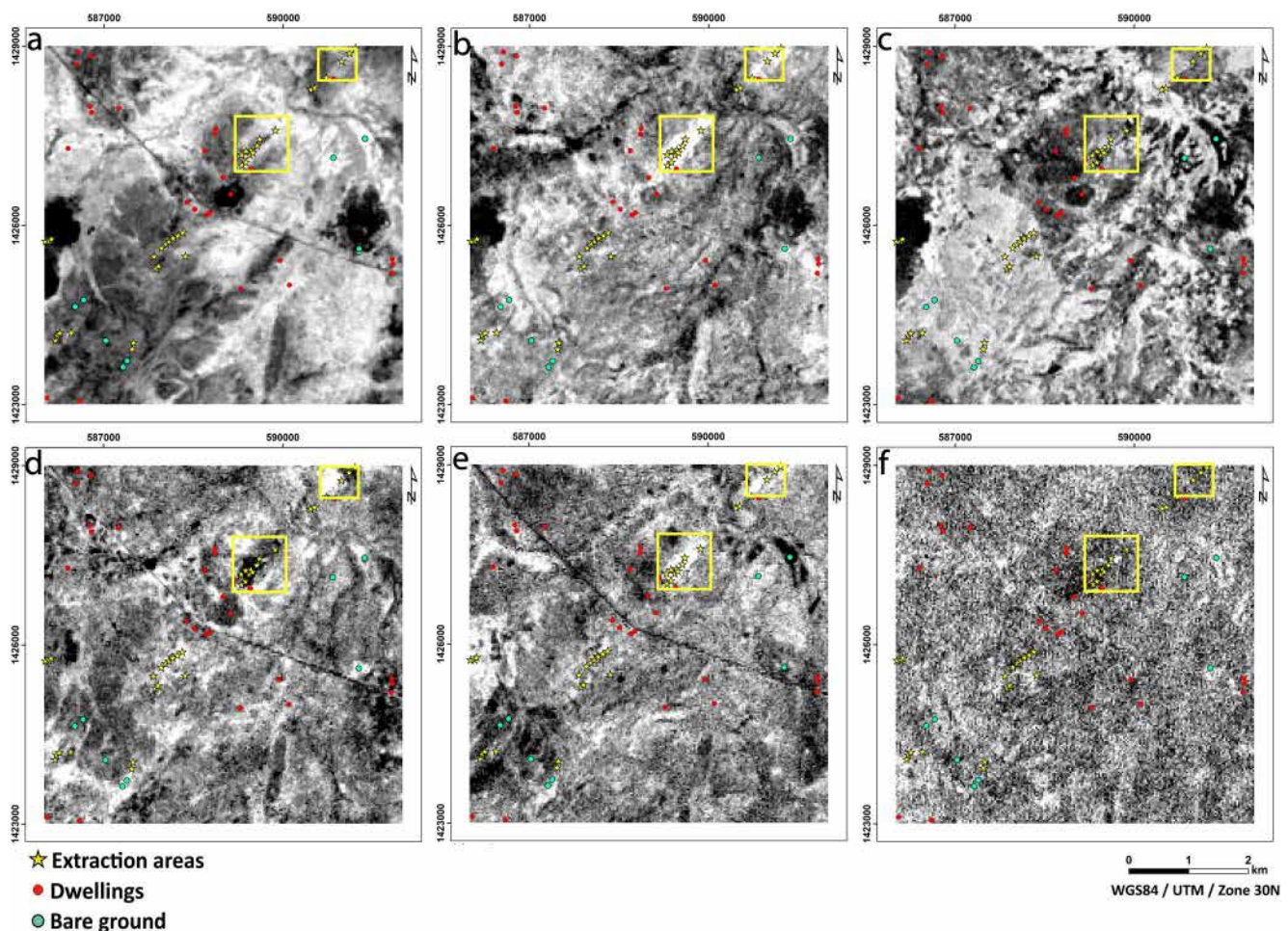


**Figure 6.** Landsat 7-ETM+ 2000 Minimum Noise Fraction (MNF) bands: (a) MNF7-1; (b) MNF7-2; (c) MNF7-3; (d) MNF7-4; (e) MNF7-5; (f) MNF7-6. The yellow square highlights the extractive areas that were already active at the time of acquisition.

**Table 4**  
MNF Band Eigenvector Matrix From Landsat 5-TM

| Eigenvectors | Band 1 | Band 2 | Band 3 | Band 4 | Band 5 | Band 6 | Eigenvalues (%) |
|--------------|--------|--------|--------|--------|--------|--------|-----------------|
| MNF5-1       | -0.694 | -0.501 | 0.197  | -0.470 | 0.019  | -0.068 | 46.69           |
| MNF5-2       | -0.689 | 0.459  | -0.445 | 0.331  | -0.025 | 0.059  | 20.20           |
| MNF5-3       | 0.174  | 0.153  | -0.628 | -0.683 | 0.282  | 0.062  | 12.53           |
| MNF5-4       | -0.100 | 0.652  | 0.604  | -0.292 | 0.324  | 0.087  | 10.83           |
| MNF5-5       | 0.025  | 0.291  | 0.026  | -0.331 | -0.852 | -0.279 | 6.32            |
| MNF5-6       | -0.001 | -0.049 | 0.035  | -0.080 | -0.296 | 0.949  | 3.41            |

• *Landsat 5-TM (year 2011)*

The eigenvectors matrix from the MNF application on the Landsat 5-TM image is shown in Table 4, whereas the MNF images are given in Figure 7. In addition to the yellow frames highlighting areas of activity in 2000, the blue frames represent new exploitation areas active in 2011 and the following years. MNF5-1 concentrates the maximum information (46.69%), followed by MNF5-2 (20.20%), MNF5-3 (12.53%), and MNF5-4 (10.83%). MNF5-5 and MNF5-6 are poor in spectral information, with 6.32% and 3.41% of eigenvalues, respectively.

The MNF5-1 does not allow discrimination between bare ground and extraction areas that both appear as white to gray pixels. In MNF5-2, the extraction area and the houses are highlighted in bright pixels. The extraction areas

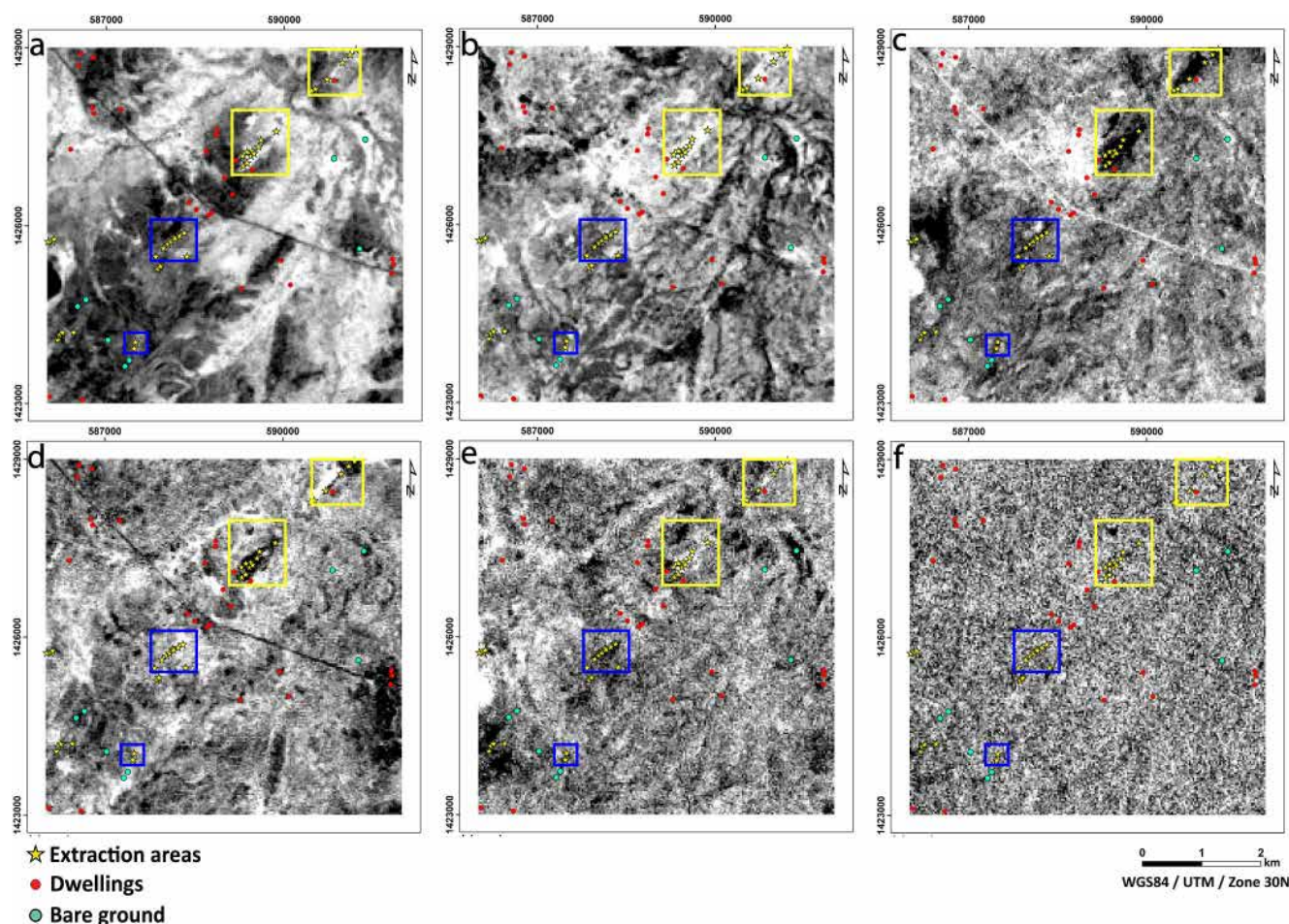


**Figure 7.** Landsat 5-TM 2011 Minimum Noise Fraction (MNF) bands: (a) MNF5-1; (b) MNF5-2; (c) MNF5-3; (d) MNF5-4; (e) MNF5-5; (f) MNF5-6. The blue square highlights the additional extractive areas already active during acquisition.



**Table 5**  
*MNF Band Eigenvector Matrix From Landsat 8-OLI*

| Eigenvectors | Band 2 | Band 3 | Band 4 | Band 5 | Band 6 | Band 7 | Eigenvalues (%) |
|--------------|--------|--------|--------|--------|--------|--------|-----------------|
| MNF8-1       | −0.210 | −0.447 | −0.285 | 0.510  | −0.082 | 0.075  | 43.96           |
| MNF8-2       | 0.013  | 0.537  | −0.317 | 0.665  | −0.239 | 0.039  | 18.35           |
| MNF8-3       | −0.585 | 0.396  | 0.541  | 0.181  | 0.346  | 0.059  | 12.77           |
| MNF8-4       | 0.393  | 0.536  | 0.010  | −0.195 | −0.258 | −0.145 | 9.34            |
| MNF8-5       | 0.524  | −0.235 | 0.668  | 0.451  | −0.076 | −0.103 | 7.50            |
| MNF8-6       | −0.410 | −0.097 | 0.161  | −0.071 | −0.635 | −0.616 | 4.79            |
| MNF8-7       | 0.119  | 0.022  | −0.226 | 0.132  | 0.581  | −0.760 | 3.27            |

are well differentiated from the dwellings in MNF5-3, with black and gray pixels, respectively. MNF5-3 gives the best results, showing extraction areas with black pixels (low pixel values). MNF5-5 and MNF5-6 are more noisy and not helpful in identifying mining sites. It is here the MNF5-3, which was retained for identifying and delineating extraction areas and monitoring the expansion of the mining activity in 2011, aided by Google imagery.

- *Landsat 8-OLI (year 2022)*

Table 5 shows the eigenvectors matrix from the MNF application on the Landsat 8-OLI image. MNF images are shown in Figure 8. In addition to the retrieval activity of 2000 and 2011, the evolution of the retrieval activity of 2022 is marked by green frames on the MNF images (Figure 8). MNF8-1 concentrates the maximum information (43.96%), followed by MNF8-2 (18.35%) and MNF8-3 (12.77%). The remaining MNFs (MNF8-4, MNF8-5, MNF8-6, and MNF8-7) show markedly reduced spectral information, with 9.34%, 7.50%, 4.79%, and 3.27% of the eigenvalues, respectively. MNF8-1 highlights mainly the dwellings and the extraction areas in black and gray pixels. The extraction areas are very well highlighted in black pixels in MNF8-2. The extraction areas are blended with the dwellings in MNF8-3–MNF8-4, with white pixels. MNF8-5 and MNF8-6 show very noisy results and cannot distinguish extraction areas from bare soils and dwellings. MNF8-2 result produced dark tones (low pixel values) for the extraction areas and was chosen to calculate the expansion of the activity in 2022.

#### 4.1.2. Estimation of the Expansion of the Extractive Activity in Time

ArcGIS 10.5 software was used to digitize the extraction areas' polygons and estimate their areas. The images MNF7-5 (2000), MNF5-3 (2011), and MNF8-2 (2022) were used for this purpose. Using Google Earth Pro 7.3 software, we refined the polygon contours for more accuracy. We divided the working area into two zones for a better perception of the analysis: the North zone (green circle in Figure 9) and the South zone (red circle in Figure 9).

For 2000, the analysis allowed us to detect two extraction sites in the North zone (Figure 9a). These two extraction sites cover 30 ha, including 20 ha for the first and 10 ha for the second sites.

2011 was marked by the detection of three additional extraction sites (Figure 9b), including one in the North zone and two in the South zone. The total area is 39.38 ha, corresponding to an increase of 9.38 ha compared to 2000. The first additional site in the North zone has an area of 3.76 ha, and the other two in the South zone have areas of 0.44 and 0.18 ha, respectively.

For 2022, we detected two additional extraction sites (Figure 9c) in the South zone, bringing the total area to 65.41 ha with an increase of 26.03 ha compared to those measured in 2011. The two additional sites cover 8.81 and 2.17 ha, respectively.

It is important to note that in addition to detecting further mining sites, there have also been fluctuations in the size of the sites identified previously. For example, the site with an area of 20 ha in 2000 increased to 20.3 ha in 2011 and then shrank to 14.3 ha in 2022. This suggests that some parts of the site are progressively abandoned, and the natural evolution of the abandoned sites leads to a spectral signature that diverges from the active mining sites. Field observations show that some abandoned sites became dwellings. Also, the site, with an area of 10 ha in

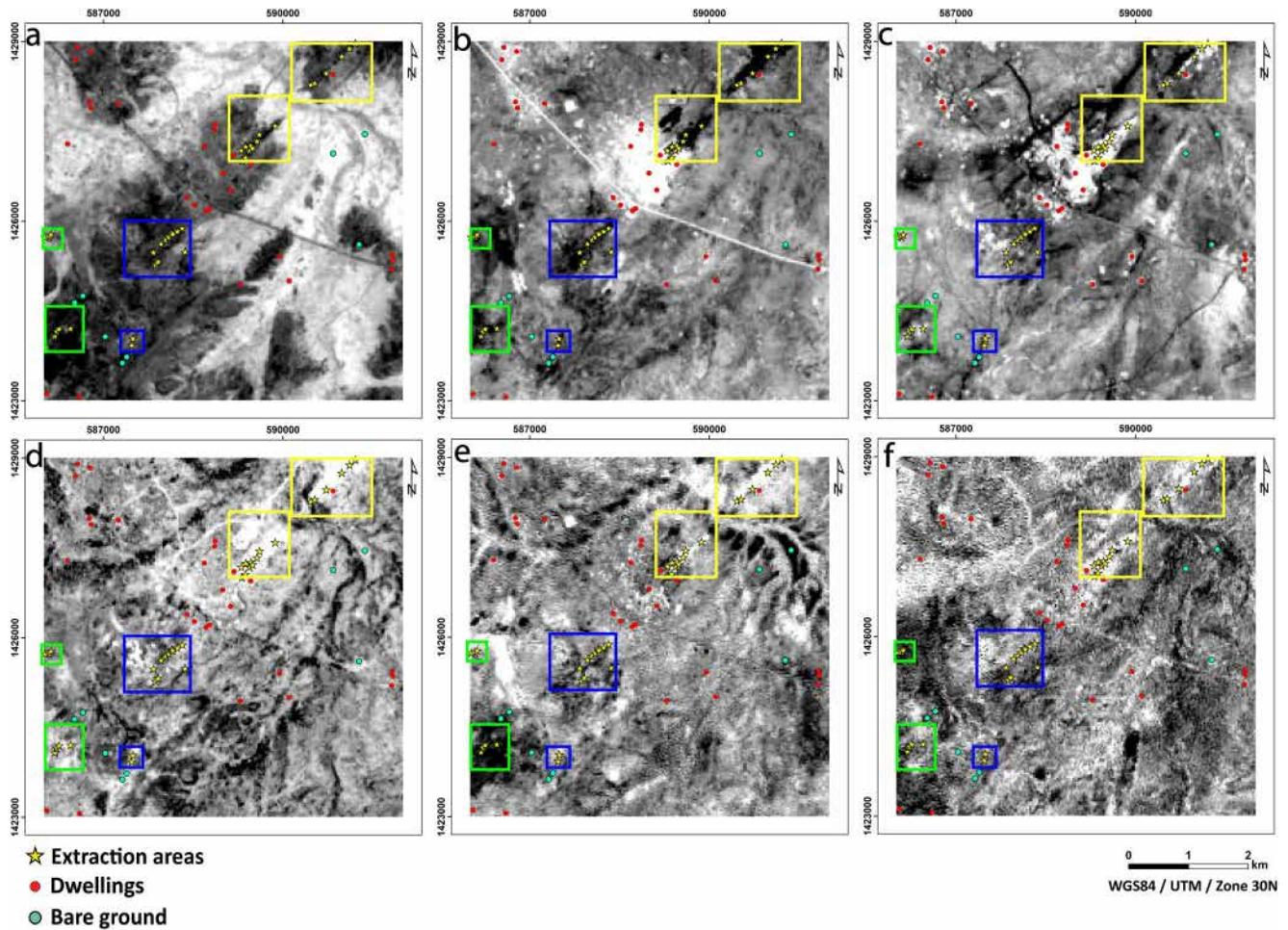


**Figure 8.** Landsat 8-OLI 2022 Minimum Noise Fraction (MNF) bands: (a) MNF8-1; (b) MNF8-2; (c) MNF8-3; (d) MNF8-4; (e) MNF8-5; (f) MNF8-6. Green square highlights the additional extractive areas that were already active at the time of acquisition.

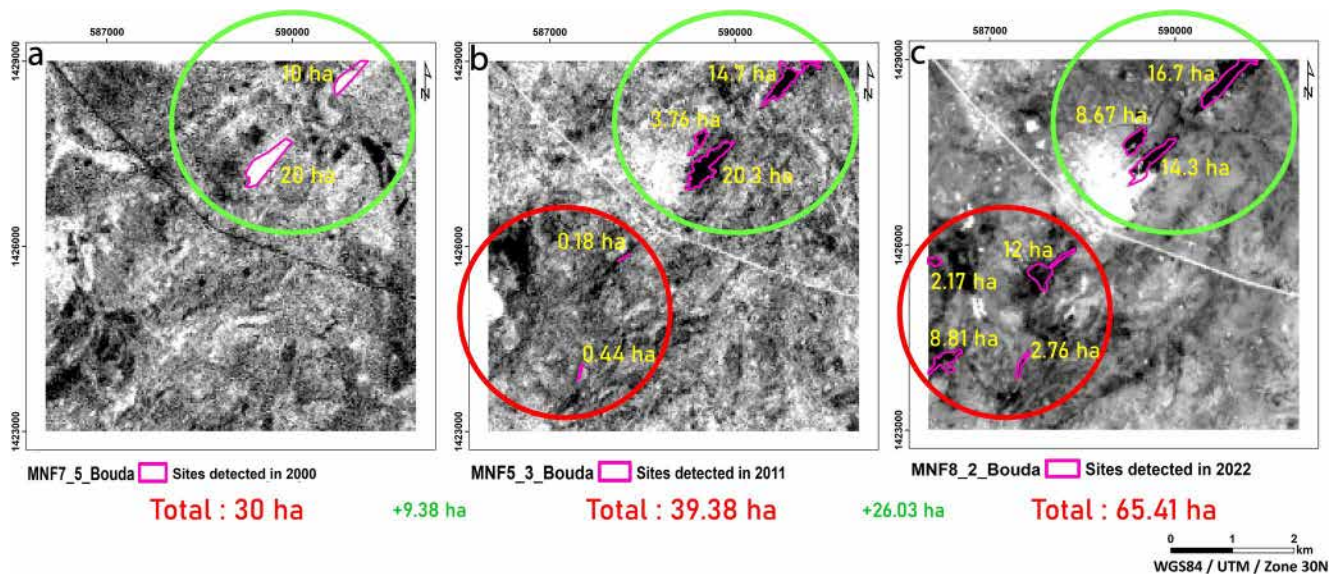


**Figure 9.** Surface progress of Bouda's mining activity over the years: (a) Year 2000; (b) Year 2011; (c) Year 2022.



**Table 6**  
*Aspect Ratios and Site Morphology Between 2000, 2011, and 2022*

| Sites | Aspect ratio 2000 | Change from 2000 to 2011 in length; width | Aspect ratio 2011 | Change from 2011 to 2022 in length; width     | Aspect ratio 2022 |
|-------|-------------------|---|-------------------|---|-------------------|
| 1     | 800/230           | Elongation<br><b>+450; +370</b>           | 1,250/600         | Elongation and regression<br><b>+30; -350</b> | 1,200/250         |
| 2     | 1,070/350         | Lateral expansion<br><b>+60; +80</b>      | 1,130/430         | Elongation and regression<br><b>-50; -180</b> | 1,080/250         |
| 3     | 0/0               | Elongation<br><b>+530; +200</b>           | 530/200           | Lateral expansion<br><b>+20; +70</b>          | 550/270           |
| 4     | 0/0               | Elongation<br><b>+240; +30</b>            | 240/30            | Elongation<br><b>+650; +440</b>               | 890/470           |
| 5     | 0/0               | Elongation<br><b>+290; +65</b>            | 290/65            | Elongation<br><b>+210; +45</b>                | 500/110           |
| 6     | 0/0               | Site does not exist                       | 0/0               | Elongation<br><b>+680; +380</b>               | 680/380           |
| 7     | 0/0               | Site does not exist                       | 0/0               | Elongation<br><b>+250; +170</b>               | 250/170           |

2000, expanded to 14.7 ha in 2011 and 16.7 ha in 2022. The three additional sites detected in 2011 have all grown from 3.76 to 8.67 ha, 0.18 to 12 ha, and from 0.44 to 2.76 ha.

In summary, the extractive activity evolves by 0.85 ha per year from 2000 to 2021, and this rate increases to 2.36 ha per year from 2011 to 2022. More specifically, we calculated independently of the North and South zones. Thus, the North zone presents an increase of 0.79 ha per year from 2000 to 2011 and 0.082 ha per year from 2011 to 2022. The South zone shows a rise of 0.056 ha per year from 2000 to 2011 and 2.28 ha from 2011 to 2022.

#### 4.1.3. Morphology of the Evolution of the Extractive Activity

We calculated the aspect ratio of the extraction sites for the morphological study. To calculate this ratio, we placed each detected site in the smallest rectangle and established the ratio of the length and width of each site. For each time interval, the aspect ratio (length/width) was calculated as the difference between the lengths and widths of the final year and the previous year. Thus, an increase in the aspect ratio is assimilated to elongation, and the opposite is incorporated into lateral expansion. Table 6 shows the different results obtained from these aspect ratio calculations. Figure 10 shows the morphology of detected sites (numbered from 1 to 7) for the years 2000, 2011, and 2022, and the numbered sites are given in Table 6, showing the aspect per time interval. Rectangles have not been drawn on Figure 10 to avoid overloading it and to perceive shape details better.

## 4.2. Results of the Lineament Analysis

### 4.2.1. Application of Band Combinations and Ratios

The band combinations 4.3.2 and 7.5.3 Landsat 8-OLI represented in RGB color images are shown in Figure 11. The band ratios 6/4.5/3.4/2, and 6/7.6/2.6/5 represented in RGB color images are shown in Figure 12. The combinations 4.3.2 and 7.5.3 do not discriminate very well the lithologies of the study area because RGB histograms (Figures 13a and 13b) show an almost equal contribution of the different bands, meaning no distinct contrasts can be perceived separating the units. This is expressed in the images by nearly monotone colors, making it impossible to discriminate between lithological units.

For Figures 13c and 13d, on the other hand, the band histograms show variations, which translate into color variation across the image (Figures 12a and 12b). This spectral contrast is more pronounced on the 6/7.6/2.6/5 combination (Figure 12b). The near-equal contribution of each band between pixel values 200–255 is probably due to the reflectance of the ore (quartz) exposed in the extraction areas because quartz is often responsible for a high albedo due to its generally light color compared to other minerals (Figure 12d). This combination was, therefore, chosen for the rest of the lineament mapping. Note that the goal is here to identify lithological

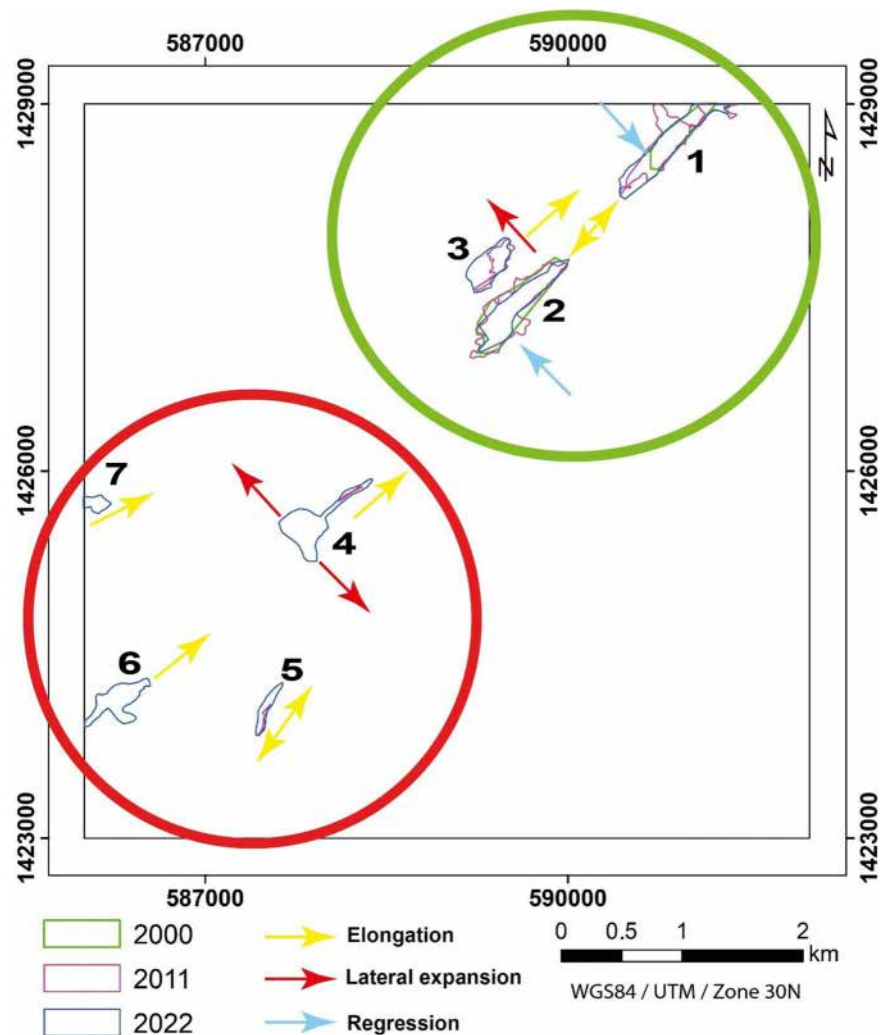


**Figure 10.** Morphological analysis of extractive activity evolution.

boundaries, but without fieldwork, it is impossible to determine the nature of the rocks within the inferred optical/lithological units.

#### 4.2.2. PCA Application

A PCA was applied to the 6/7.6/2.6/5 band ratio combination image to perform a lineament mapping of the study area. Table 7 shows the eigenvectors matrix from the PCA application. The spectral information is concentrated in the first principal component (PC1) (Figure 14a), with 67.73% of the spectral information assumed to be related to the lithology (Table 7). The other principal components (PC2 and PC3) lack spectral data (Figures 14b and 14c), with 19.38% and 12.88% of the eigenvalues, respectively. PC1, concentrating 67.73% of the spectral information, has been used to extract the lineaments in the study area.

#### 4.2.3. Application of Directional Filters

The application of directional filters is intended to facilitate identifying and tracking lineaments corresponding to lithological or structural discontinuities in the images. Directional filters improve the perception of lineaments. In addition, this type of filter can highlight lineaments not favored by the illumination source. In our study, the enhancement of the lineaments was performed on the PC1 image shown in Figure 15 with the directional filters following the directions of 0°, 45°, 90°, and 135°.

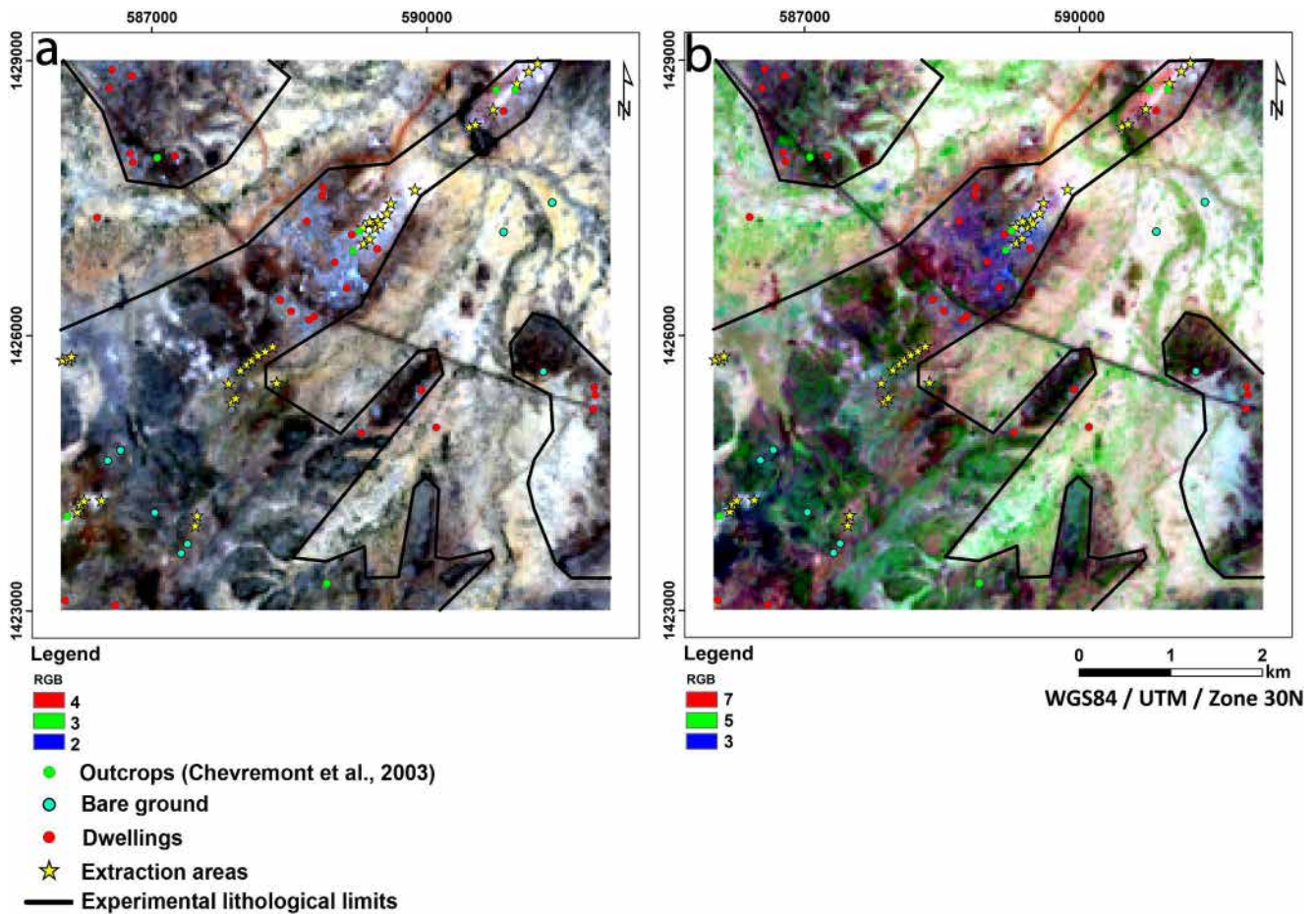


Figure 11. RGB combinations of bands: (a) 4.3.2 combination; (b) 7.5.3 combination.

#### 4.2.4. Extraction and Lineament Analysis

For each filter direction, lineaments were automatically extracted using the “Line Extraction” module of the PCI Geomatica 2013 software. Thus, Figures 15a–15d show the extracted lineaments overlain on the corresponding directional filter. Also, three lineaments were added manually after a double-check. At the end of this process, a lineament map (Figure 16) was produced by merging extracted lineaments, when relevant, and removing remaining artifacts (duplicated tracks, roads). Thus, in a decreasing order, we have 209 lineaments for the NW-SE direction, 197 for the N-S direction, and 191 and 186 lineaments, respectively, for the NE-SW and E-W directions for a total of 783 lineaments extracted.

The directional rosette shows lineament directions weighted by their lengths (Figure 17). The predominant direction is NE-SW, followed by N-S. However, the directions of short lineaments are distributed relatively homogeneously (no preferential direction). The lineament density map overlain on the extraction areas reveals that high lineament densities correlate with known gold occurrences (Figure 18). The high lineament densities are elongated in the primary NE-SW mining direction.

### 5. Discussions

This study shows that the near and shortwave infrared bands (NIR and SWIR 1) significantly contribute to detecting ore extraction areas in artisanal gold mining. MNF application on Landsat 7-ETM+, 5-TM, and 8-OLI images show that the MNFs chosen for the spatiotemporal analysis present a better detection of the extraction areas for a strong negative weighting of the near-infrared band for Landsat 7-ETM+ (−0.757) and a moderate positive weighting of the near-infrared band for Landsat 5-TM (0.282). The shortwave infrared band for Landsat 8-OLI (0.665) shows a strong positive weighting. The strong positive weights are marked by a low value of the



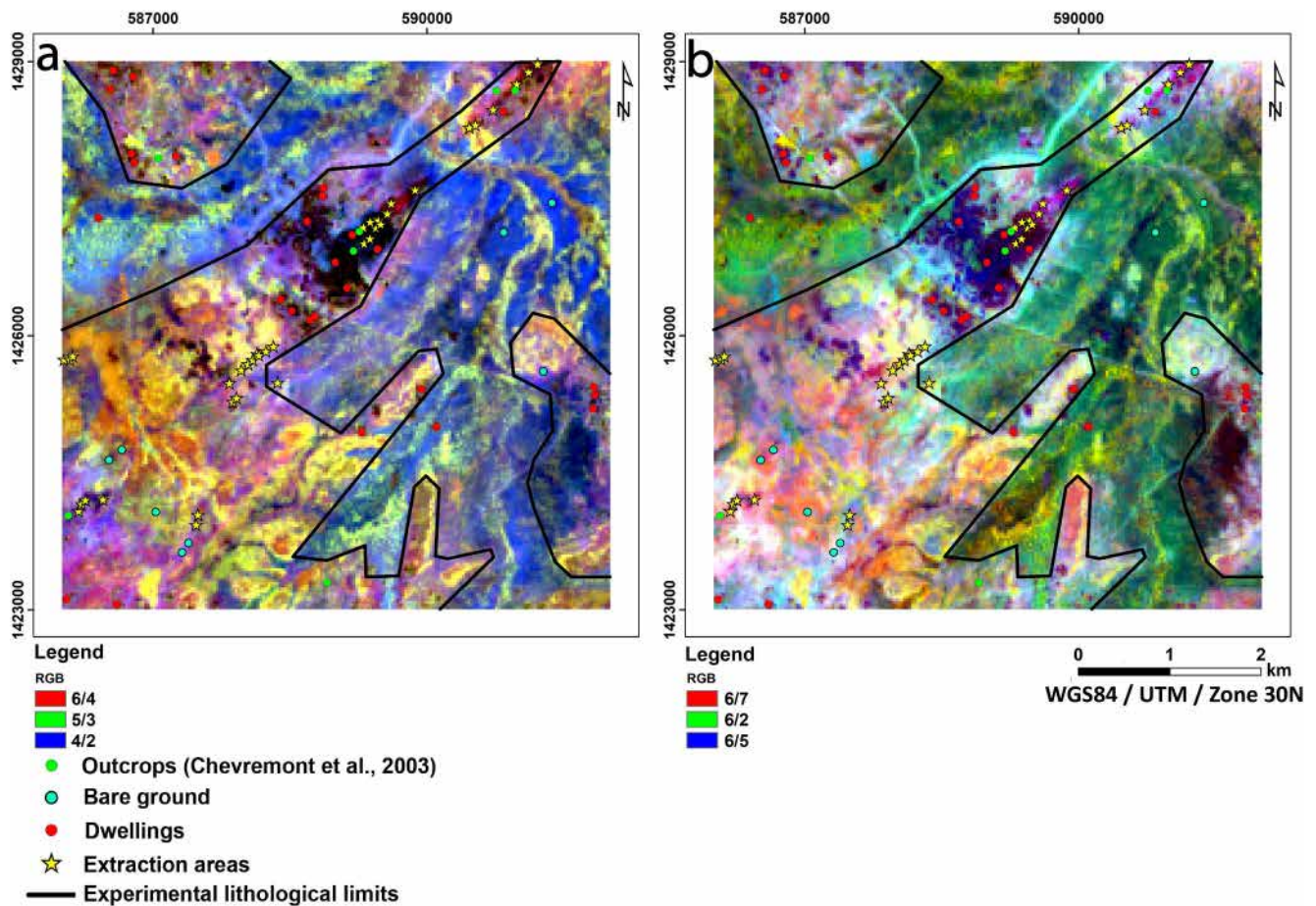


**Figure 12.** RGB combinations of bands: (a) 6/4.5/3.4/2 combination; (b) 6/7.6/2.6/5 combination.

extraction areas (black pixels), whereas the strong negative weights show a high value of the extraction areas (white pixels). Several previous studies have demonstrated the contribution of the NIR and SWIR 1 band in lithologic mapping through the absorption and reflectance of rock materials in the NIR-SWIR 1 domain (Abass Saley et al., 2021; Ghislain et al., 2021; Gomez, 2004).

Several methodologies for artisanal mining activity monitoring from remote sensing data have been explored recently and rely on various techniques, including those used in the current study and more sophisticated approaches using artificial intelligence (Abass Saley et al., 2021; Forkuor et al., 2020; Ngom et al., 2020). The methodology tested here was chosen to demonstrate its simplicity of use, which is critical for routine use beyond the academic domain by actors of the governance of the mining sector with various backgrounds and who may be trained based on limited expertise in remote sensing analyses. Unlike previous work on this subject using a panoply of field data, Burkina Faso's context of insecurity makes it impossible to collect the desired amount of field data. This methodology could contribute to decision-making regarding monitoring artisanal mining sites and a tool for exploring additional favorable zones.

Based on an analysis of the progress of mining activity, the main factor influencing the fluctuation in the size of the extraction areas is gold price Abass Saley et al. (2021). In this respect, gold price affects industrial and artisanal mining similarly. Specifically, between 2000 (US\$282 in January 2000) and 2011 (US\$1873 in August 2011), extraction in the North zone evolved with gold price until the peak of gold price between 2011 and 2022 (US\$2051 in March 2022). At this point, mining activity in the North zone slowed down and transitioned to the South zone.

Analysis of the morphology of mining activity evolution reveals a progressive elongation of the extraction sites in an NE-SW direction. This direction is identical to the predominant direction shown by lineament analysis.



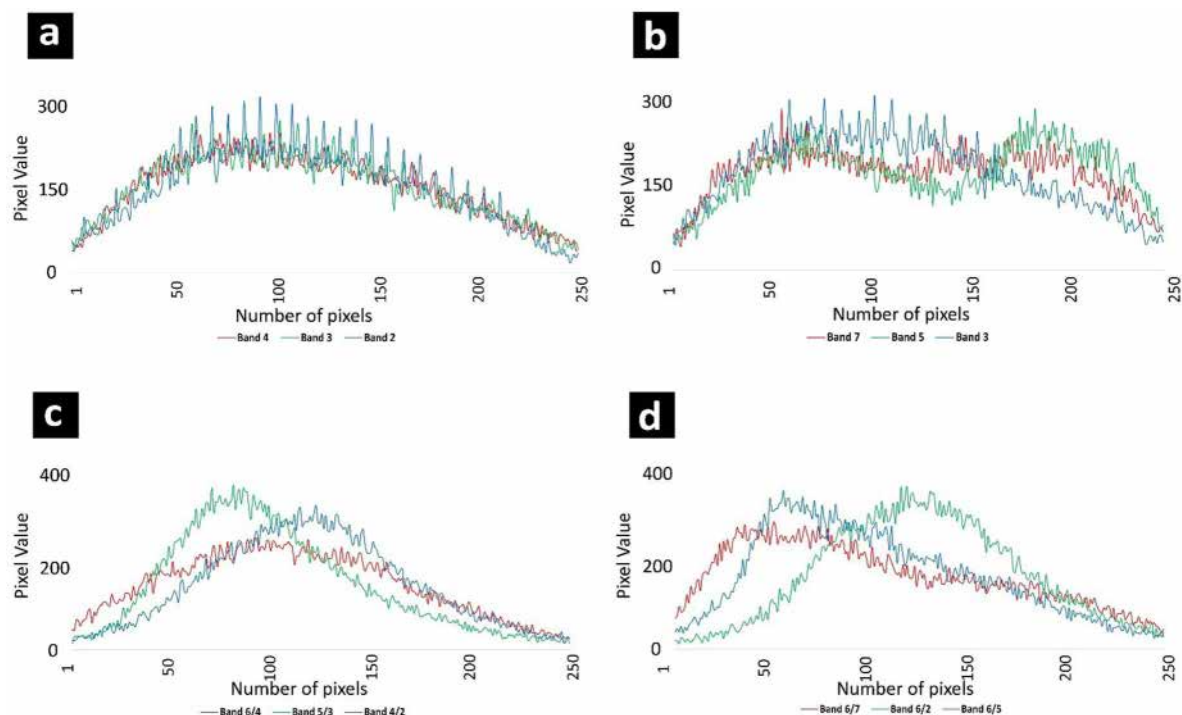


**Figure 13.** Band histograms for the different RGB combinations tested: (a) 4.3.2 combination; (b) 7.5.3 combination; (c) 6/4.5/3.4/2 combination; (d) 6/7.6/2.6/5 combination.

Fieldwork provided information on the gold mineralization, hosted in sheared and laminated quartz veins that are NE-SW trending. The field data confirms that the direction of the extraction sites and the gold-bearing quartz veins are similar. In contrast, the spatiotemporal analysis suggests the continuity and parallelism of the gold-bearing quartz veins between the North and South Zone sites. The NE-SW direction of the gold-bearing mining sites, schistose metasediments, and quartz veins is consistent with the significant deformation phase D1 of the Eburnean orogeny previously identified in the Man-Leo Ridge (Baratoux et al., 2011; Chevremont et al., 2003; Feybesse et al., 1990, 2006; Milesi et al., 1992) and related to a NW-SE to WNW-ESE regional compression. These directions are consistent with the orientations described by Baratoux et al. (2011) associated with D1 and D2, with most gold mineralization related to the D2 transpressional event. The lineament density map shows a structural control on the expansion of artisanal gold activity at the Bouda site (Figure 18). The areas with high lineament densities are elongated in the primary NE-SW mining direction and match the known gold occurrences well.

Based on the spatiotemporal and lineament analyses of the Bouda site, we propose five prospecting corridors based on the continuity and parallelism of the extraction zones (North and South) and their correlation with lineament densities (Figure 18). The use of remote sensing tools for exploration is promising but cannot entirely replace field investigations (Augustin & Gaboury, 2017; Baratoux et al., 2011; Ilboudo et al., 2017, 2018; Naba, 2007). As a result, the five prospecting corridors will need to be verified or field-checked in a more favorable security context to confirm the continuity of the mineralization at the Bouda site. Also, another remote sensing study is still in progress on the Bouda site. It will allow us to further constrain the prospecting corridors' potential by surveying hydrothermal alteration by remote sensing and ASD spectrometry.

**Table 7**  
PC Band Eigenvector Matrix

| Eigenvectors | Band 1 | Band 2 | Band 3 | Eigenvalues (%) |
|--------------|--------|--------|--------|-----------------|
| PC1          | -0.686 | -0.499 | -0.529 | 67.736          |
| PC2          | -0.603 | -0.015 | 0.796  | 19.383          |
| PC3          | 0.405  | -0.866 | 0.290  | 12.881          |

The proposed exploration corridors were overlain on the topographic map of the study area (Figure 19). We noted that topographic knolls are associated with regions of high lineament density. There is a possible bias in this observation since low-lying areas may sometimes be covered by colluvium and alluvium, which might lead to an underestimation of lineaments in low

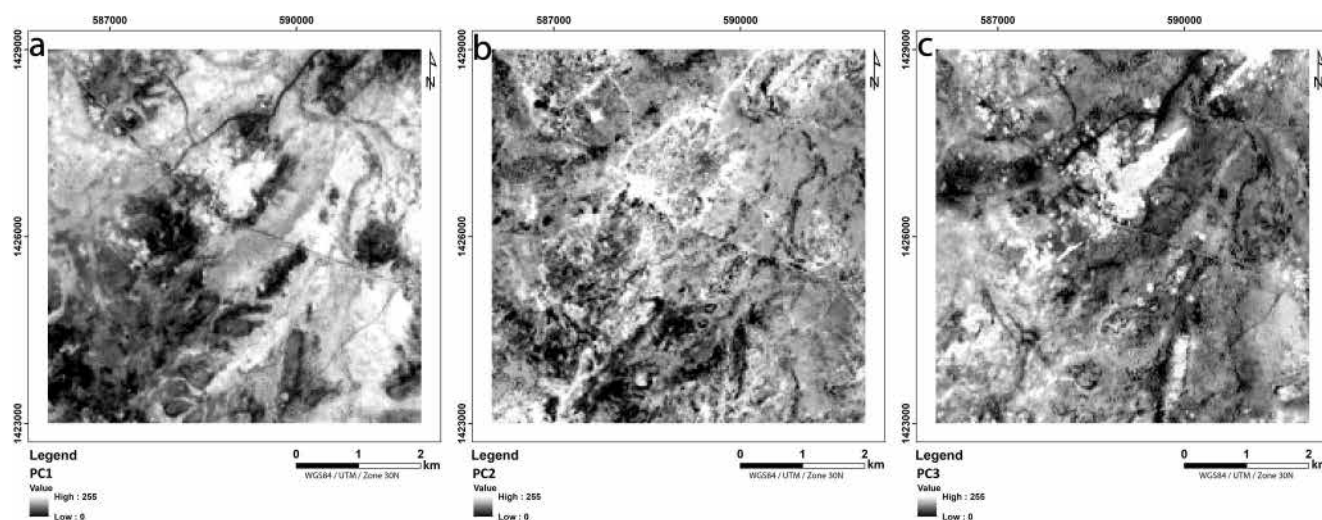


**Figure 14.** Principal Components Analysis on 6/7.6/2.6/5 combination: (a) PC1; (b) PC2; (c) PC3.

areas. The link between topographic knolls, lineaments, and mineralization may alternatively, and more likely, in our opinion, reflect processes, such as silicification, that both lead to the formation of these knolls (resistance to erosion) and mineralization. Topographic knolls can act as markers of mineralization zones, their association faults or fractures offering pathways for siliceous hydrothermal fluids involved in the mineralization. For example, the tectonic processes that lead to the formation of knolls can also create favorable conditions for mineralization, such as the presence of hydrothermal fluids.

Considering the insecurity that Burkina Faso has been experiencing since 2015, it is difficult for the authorities to prevent illegal exploitation and the expansion of illegal mining sites. The methodology used is inexpensive and well suited to the Sahelian and economic context of Burkina Faso, as the satellite images used are free and downloadable online. Burkina Faso generally has low cloud cover, except during the rainy season, which is neither favorable to geological exploration nor exploitation, so this methodology applies almost all year round. It is possible to develop online applications for monitoring artisanal gold mining, as is the case for Senegal (Ngom, 2022). With its geological exploration aspect, this methodology shows the possibility of defining relevant exploration targets that could ensure the long-term operation of these artisanal mining sites, which could eventually evolve into semi-mechanized operations. By supporting the development of a minor sector toward semi-mechanized operations, the government could undertake a system of community entrepreneurship where each gold miner could be a shareholder. This system would create a relationship of trust between gold miners and the government and provide solutions for better organization of artisanal gold mining in Burkina Faso and better regulation of operations, revenues, taxes and environmental impacts and remediation procedures. This will require collaboration between the academia, the Ministry in charge of mines, and the gold miners. The results achieved by this study with so little field data and publicly available satellite images are very encouraging. We anticipate even better results with higher spatial or spectral Earth observation products. This study, among others, illustrates the potential benefits of enhancing the uptake of Earth Observation products and services in Africa through interdisciplinary approaches (Speranza et al., 2022).

## 6. Conclusion

This study contributes to geological exploration in a context of insecurity, pushing the interpretation of remote sensing data sets to the limits. Our approach using spatial data has allowed us to highlight the structural control of artisanal gold activity at the Bouda site. On the one hand, MNF allowed the detection of extraction sites and a spatiotemporal analysis. On the other hand, PCA and band combinations/ratios contributed to a lineament analysis. This is less costly and fast enough for mineral exploration. This study demonstrates that space-borne tools may be developed in Burkina Faso to support the development of regulated artisanal and semi-mechanized mining sectors.

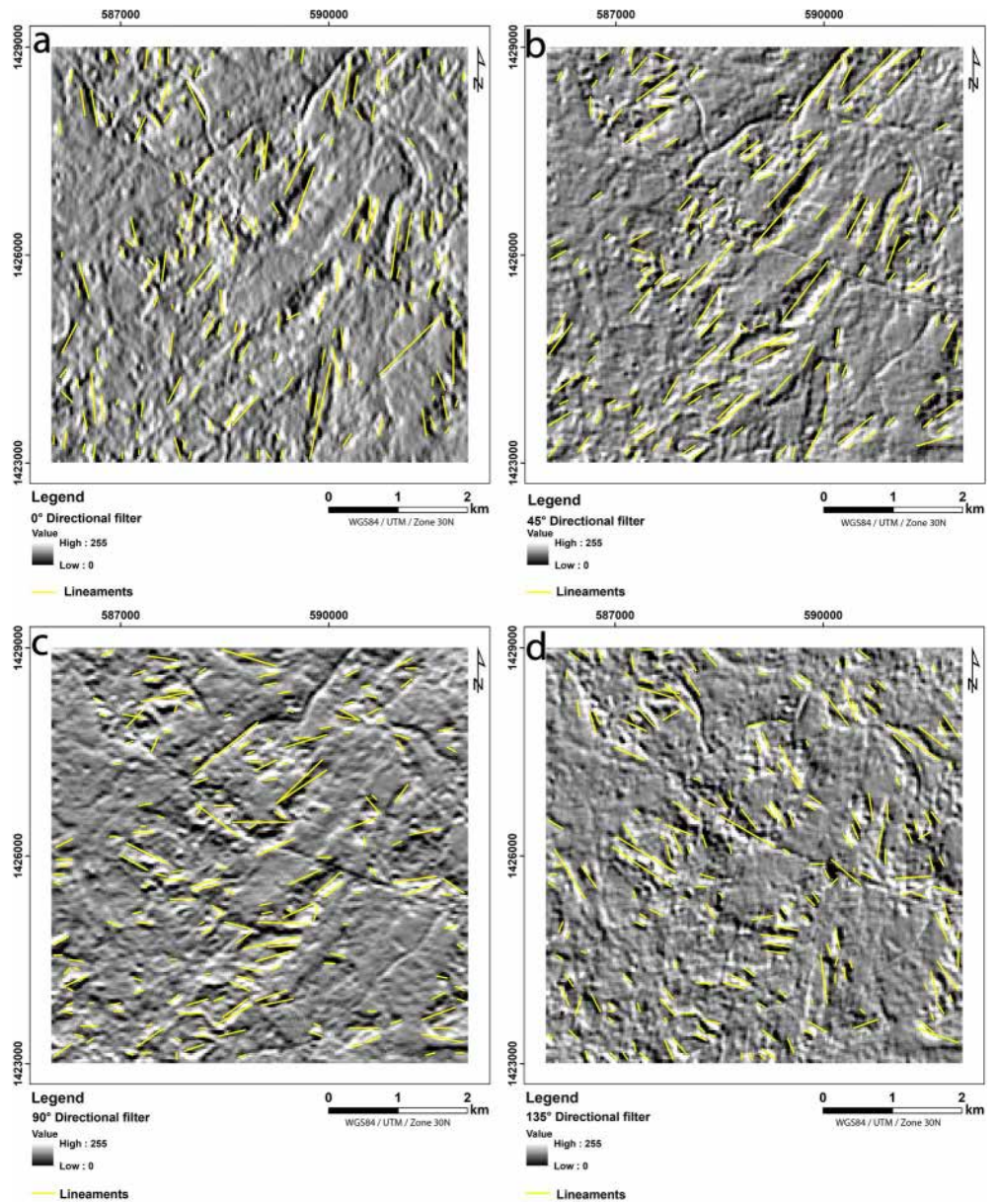


**Figure 15.** Directional filters overlaid on the corresponding extracted lineaments: (a) 0°; (b) 45°; (c) 90°; (d) 135°.

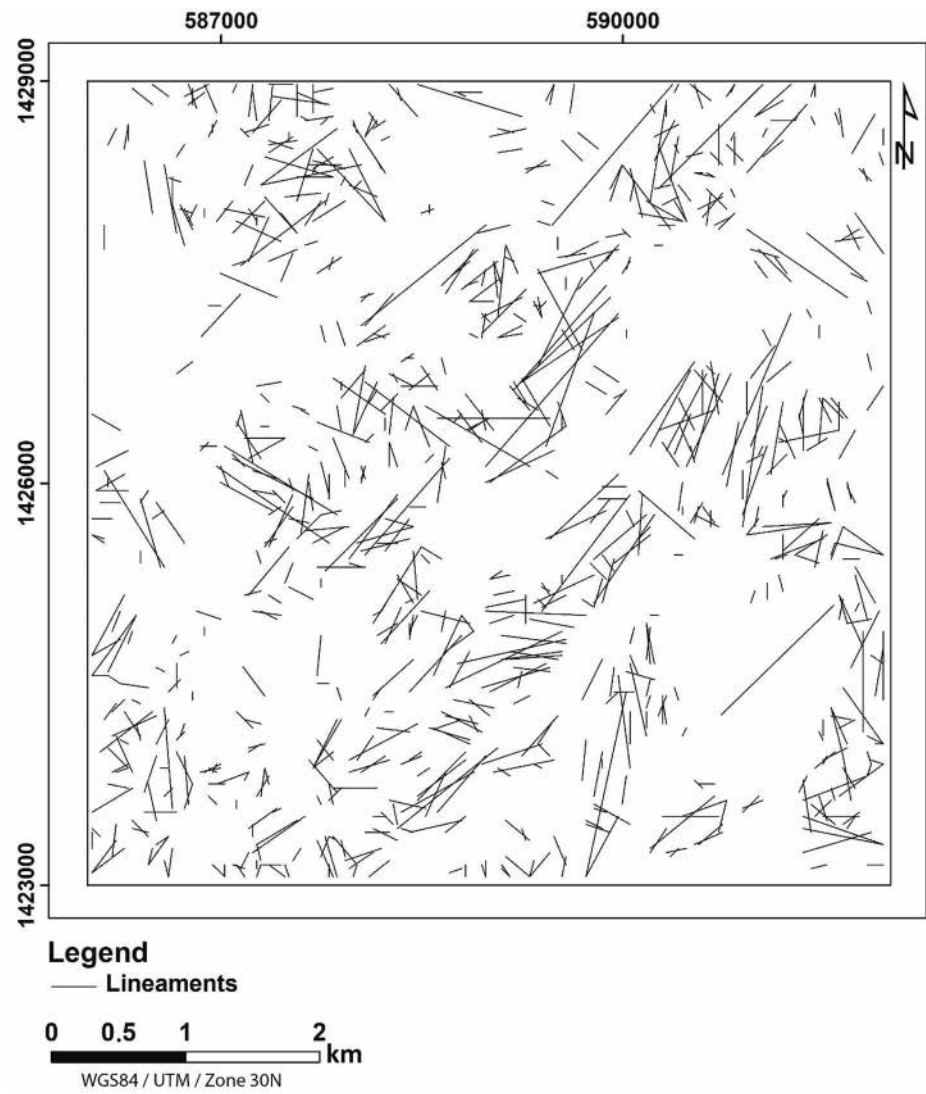


**Figure 16.** Lineament map.



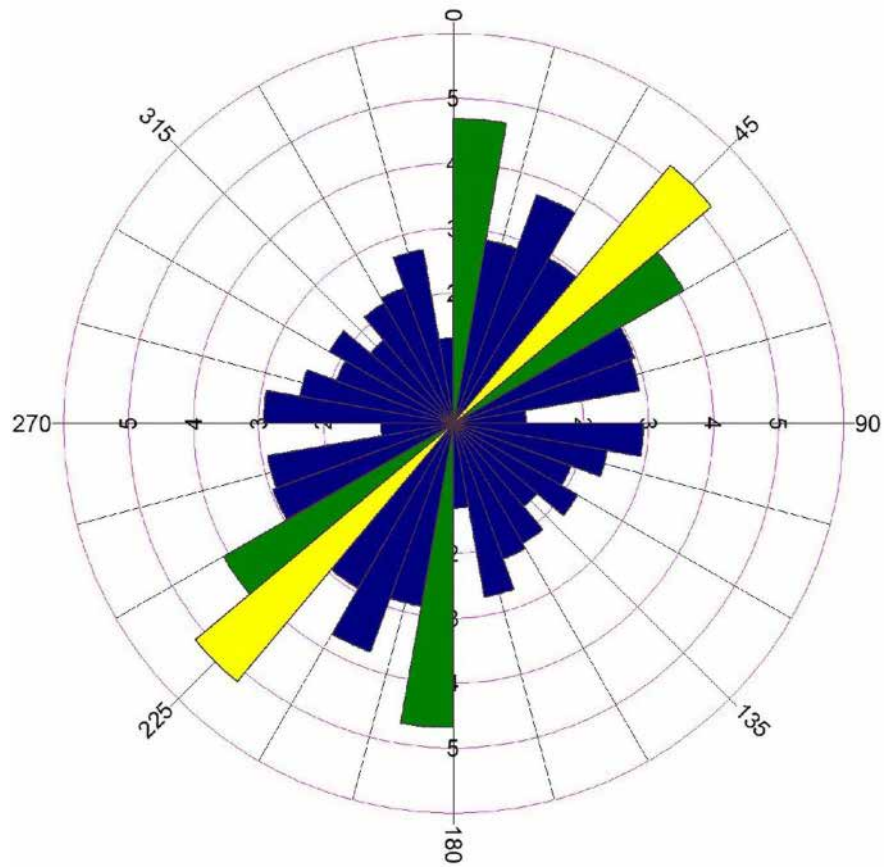


**Figure 17.** Directional rosette showing length-weighted lineament directions.

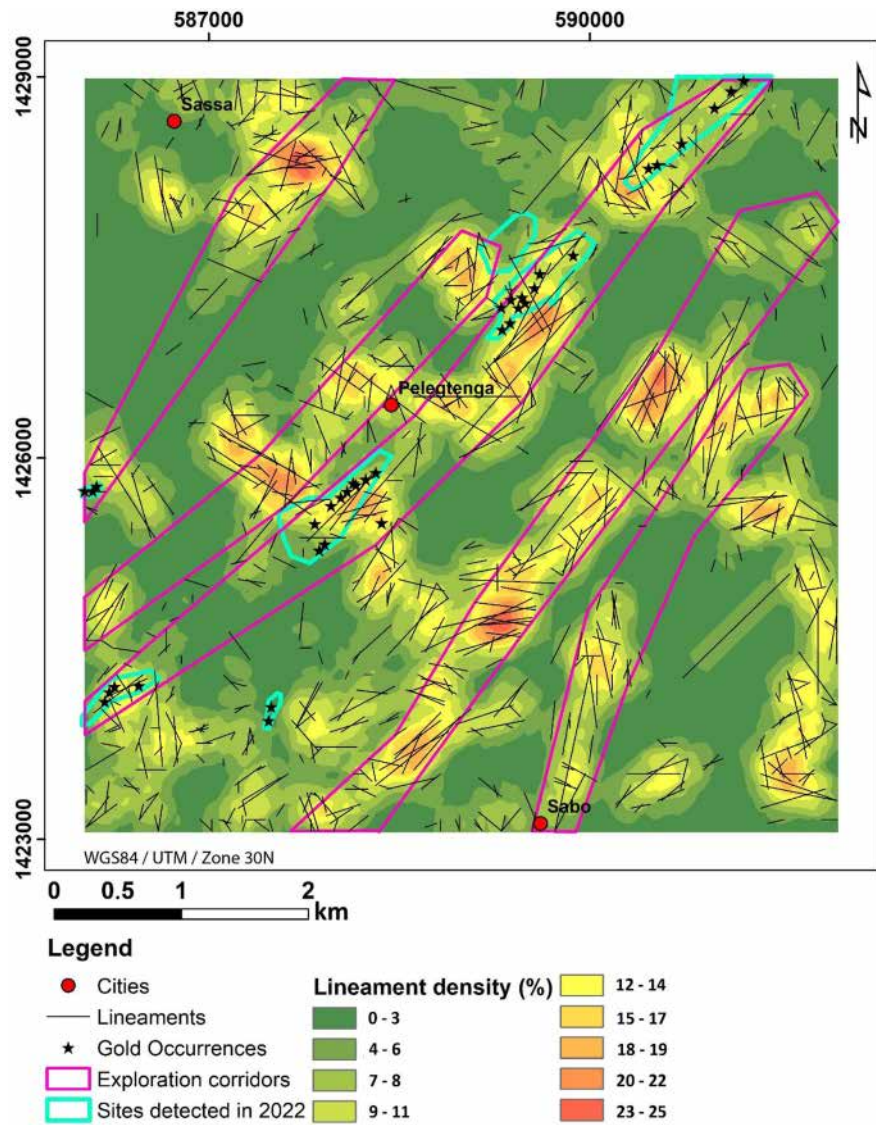


**Figure 18.** Prospective map defining exploration corridors. Lineament density is overlain on extraction zones and lineaments.

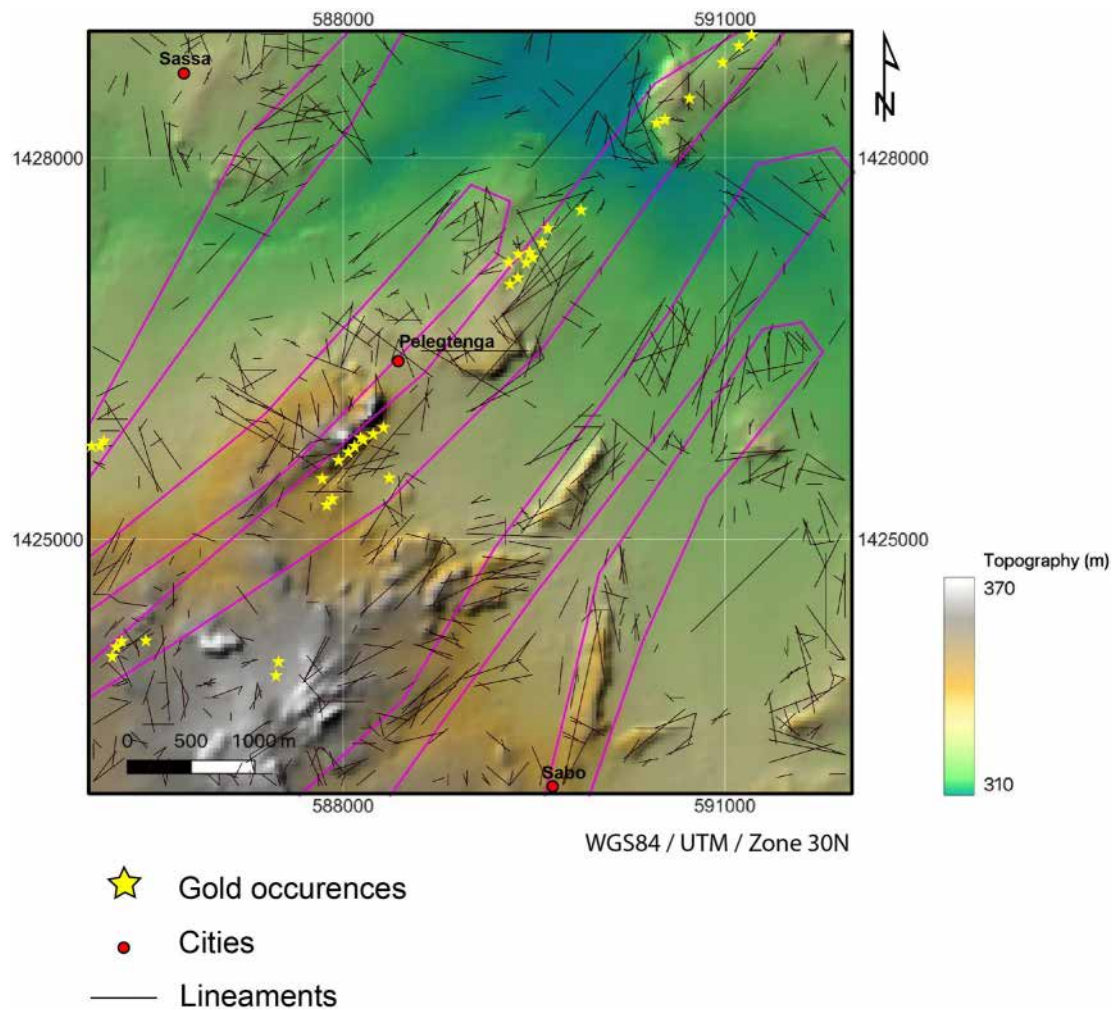


**Figure 19.** Exploration corridors overlaid on the topography of the study area.

### Conflict of Interest

The authors declare no conflicts of interest relevant to this study.

### Data Availability Statement

This manuscript uses publicly available Landsat 5, 7, and 8 data, downloaded from the USGS server <http://earthexplorer.usgs.gov>. Landsat 5 Scene ID: LT51950512011039MPS00. Landsat 7 Scene ID: LE71950512000049EDC00. Landsat 8 Scene ID: LC81950512022117LGN00.

### References

- Abass Saley, A., Baratoux, D., Baratoux, L., Ahoussi, K. E., Yao, K. A., & Kouamé, K. J. (2021). Evolution of the Koma Bangou gold panning site (Niger) from 1984 to 2020 using Landsat imagery. *Earth and Space Science*, 8(11), e2021EA001879. <https://doi.org/10.1029/2021EA001879>
- Abdessamad, E. A., Zine, E. E., & Mustapha, S. (2018). Utilisation de l'image multispectrale pour l'exploration et la recherche des ressources minérales: Etat des connaissances et proposition d'un modèle de traitement. *European Scientific Journal*, 14(24), 350. <https://doi.org/10.19044/esj.2018.v14n24p350>
- Adiri, Z., El Harti, A., Jellouli, A., Maacha, L., & Bachaoui, E. (2016). Lithological mapping using Landsat 8-OLI and Terra ASTER multispectral data in the Bas Drâaa inlier, Moroccan Anti Atlas. *Journal of Applied Remote Sensing*, 10(1), 016005. <https://doi.org/10.1117/1.JRS.10.016005>
- Adiri, Z., Lhissou, R., El Harti, A., Jellouli, A., & Chakouri, M. (2020). Recent advances in the use of public domain satellite imagery for mineral exploration: A review of Landsat-8 and Sentinel-2 applications. *Ore Geology Reviews*, 117, 103332. <https://doi.org/10.1016/j.oregeorev.2020.103332>

### Acknowledgments

This work was made possible by financial support from the Agate project, Burkina Faso Higher Education Support Project (PAES), Institute of Research for Development (IRD), and Toulouse Graduate School of Earth and Space Science (TESS). The authors would like to thank each structure for its contribution to the success of this work. The authors thank the Laboratory for Responsible Mining in West Africa (LMI MINERWA, <https://miner-wa.org>) and the TEGECO group for their scientific and technical support. We would like to thank the reviewers and the associate editor. Their contribution improved an earlier version of this manuscript.



- Amer, R., Kusky, T., & El Mezayen, A. (2012). Remote sensing detection of gold related alteration zones in Um Rus area, central eastern desert of Egypt. *Advances in Space Research*, 49(1), 121–134. <https://doi.org/10.1016/j.asr.2011.09.024>
- Aretouyap, Z., Billa, L., Jones, M., & Richter, G. (2020). Geospatial and statistical interpretation of lineaments: Salinity intrusion in the Kribi-Campo coastland of Cameroon. *Advances in Space Research*, 66(4), 844–853. <https://doi.org/10.1016/j.asr.2020.05.002>
- Augustin, J., & Gaboury, D. (2017). Paleoproterozoic plume-related basaltic rocks in the Mana gold district in western Burkina Faso, West Africa: Implications for exploration and the source of gold in orogenic deposits. *Journal of African Earth Sciences*, 129, 17–30. <https://doi.org/10.1016/j.jafrearsci.2016.12.007>
- Aziz, O., Ousmane, B., Gbélé, O., Eric, G., & Saga, S. (2016). Caractérisations structurales des gîtes aurifères du corridor de Bou Boulou-Bouda au Burkina Faso, Afrique de l'Ouest. *Afrique Science*, 12(5), 89–104.
- Baratoux, L., Metelka, V., Naba, S., Jessell, W. M., Gregoire, M., & Ganne, J. (2011). Juvenile Paleoproterozoic crust evolution during the Eburnean orogeny (~2.2–2.0 Ga), western Burkina Faso. *Precambrian Research*, 191(1–2), 18–45. <https://doi.org/10.1016/j.precamres.2011.08.010>
- Bedini, E. (2011). Mineral mapping in the Kap Simpson complex, central East Greenland, using HyMap and ASTER remote sensing data. *Advances in Space Research*, 47(1), 60–73. <https://doi.org/10.1016/j.asr.2010.08.021>
- Bedini, E. (2017). The use of hyperspectral remote sensing for mineral exploration: A review. *Journal of Hyperspectral Remote Sensing*, 7(4), 189–211. <https://doi.org/10.29150/jhrs.v7.4.p189-211>
- Chevremont, P., Donzeau, M., Le Metour, J., Koté, S., Ouédraogo, I., Kabore, E. B., et al. (2003). Carte géologique du Burkina Faso à 1/200 000, feuille Koudougou.
- de Kock, G. S., Théveniaut, H., Botha, P. M. W., & Gyaopong, W. (2012). Timing the structural events in the Paleoproterozoic Bole-Nangodi belt terrane and adjacent Maluwe basin, West African craton, in central-west Ghana. *Journal of African Earth Sciences*, 65, 1–24. <https://doi.org/10.1016/j.jafrearsci.2011.11.007>
- Dubois, J. (1999). *Identification des linéaments dans les images satellitaires par ajustement et suivi de segments*. (p. 123). Projet appliqué Maitrise. Université du Québec.
- Endyana, C., Sukiyah, E., & Dharmawan, I. A. (2018). Fracture analysis to delineate tectonic evolution: Case study at Ciharang, Bogor-Sukabumi, West Java, Indonesia. In *Journal of physics: Conference series* (Vol. 1080, p. 012036). <https://doi.org/10.1088/1742-6596/1080/1/012036>
- Feybesse, J. L., Billa, M., Guerot, C., Duguey, E., Lescuyer, J. L., Milési, J. P., & Bouchot, V. (2006). The Paleoproterozoic Ghanaian province. Geodynamic model and ore controls, including regional stress modelling. *Precambrian Research*, 149(3–4), 149–196. <https://doi.org/10.1016/j.precamres.2006.06.003>
- Feybesse, J. L., Milési, J. P., Ouédraogo, M. F., & Prost, A. (1990). La ceinture protérozoïque inférieure de Boromo–Goren (Burkina Faso): un exemple d'interférence entre deux phases transcurrentes éburnéennes. *Comptes Rendus de L'Académie des Sciences*, 310(II), 1353–1360.
- Forkuor, G., Ullmann, T., & Griesbeck, M. (2020). Mapping and monitoring small-scale mining activities in Ghana using Sentinel-1 time series (2015–2019). *Remote Sensing*, 12(6), 911. <https://doi.org/10.3390/rs12060911>
- Ganne, J., De Andrade, V., Weinberg, R. F., Vidal, O., Dubacq, B., Kagambega, N., et al. (2012). Modern-style plate subduction preserved in the Paleoproterozoic West African craton. *Nature Geoscience*, 5(1), 60–65. <https://doi.org/10.1038/ngeo1321>
- Gannouni, S., & Gabtni, H. (2015). Structural interpretation of lineaments by satellite image processing (Landsat TM) in the region of Zahret Medien (northern Tunisia). *Journal of Geographical Systems*, 7(02), 119–127. <https://doi.org/10.4236/jgis.2015.72011>
- Ghislain, N. M., Timoleon, N., Jonas, D. T. W., Sylvestre, G., Pour, A. B., Patrick, A. K., et al. (2021). Remote sensing satellite-based structural/alteration mapping for gold exploration in the Kett'e goldfield, Eastern Cameroon. *Journal of African Earth Sciences*, 184, 104386. <https://doi.org/10.1016/j.jafrearsci.2021.104386>
- Girija, R. R., & Mayappan, S. (2019). Mapping of mineral resources and lithological units: A review of remote sensing techniques. *International Journal of Image and Data Fusion*, 10(2), 79–106. <https://doi.org/10.1080/19479832.2019.1589585>
- Goldfarb, R. J., André-Mayer, A.-S., Jowitt, S. M., & Mudd, G. M. (2017). West Africa: The world's premier Paleoproterozoic gold province. *Economic Geology*, 112(1), 123–143. <https://doi.org/10.2113/econgeo.112.1.123>
- Gomez, C. (2004). *Potentiels des données de télédétection multisources pour la cartographie géologique: Application à la région de Rehoboth (Namibie)*. Traitement du signal et de l'image [eess.SP]. Université Claude Bernard—Lyon I. Retrieved from <https://theses.hal.science/tel-00008556>
- Green, A. A., Berman, M., Switzer, P., & Craig, M. D. (1988). A transformation for ordering multispectral data in terms of image quality with implications for noise removal. *IEEE Transactions on Geoscience and Remote Sensing*, 26(1), 65–74. <https://doi.org/10.1109/36.3001>
- Grenholm, M. (2014). The Birimian event in the Baoulé Mossi domain (West African Craton) regional and global context. PhD Thesis (p. 116). Lund University.
- Grenholm, M., Jessell, M., & Thébaud, N. (2019). A geodynamic model for the Paleoproterozoic (ca. 2.27–1.96 Ga) Birimian Orogen of the southern West African Craton—Insights into an evolving accretionary-collisional orogenic system. *Earth-Science Reviews*, 192, 138–193. <https://doi.org/10.1016/j.earscirev.2019.02.006>
- Han, L., Liu, Z., Ning, Y., & Zhao, Z. (2018). Extraction and analysis of geological lineaments combining a DEM and remote sensing images from the northern Baoji loess area. *Advances in Space Research*, 62(9), 2480–2493. <https://doi.org/10.1016/j.asr.2018.07.030>
- Hein, K. A. A., Morel, V., Kagoné, O., Kiemde, F., & Mayes, K. (2004). Birimian lithological succession and structural evolution in the Goren segment of the Boromo–Goren greenstone belt, Burkina Faso. *Journal of African Earth Sciences*, 39(1–2), 1–23. <https://doi.org/10.1016/j.jafrearsci.2004.05.003>
- Hilson, G. (2020). The Africa mining vision: A manifesto for more inclusive extractive industry-led development? *Canadian Journal of Development Studies/Revue Canadienne d'Études du Développement*, 41(3), 417–431. <https://doi.org/10.1080/02255189.2020.1821352>
- Hirdes, W., Davis, D. W., Lüdtke, G., & Konan, G. (1996). Two generations of Birimian (Paleoproterozoic) volcanic belts in north-eastern Côte d'Ivoire (West Africa): Consequences for the 'Birimian controversy'. *Precambrian Research*, 80(3–4), 173–191. [https://doi.org/10.1016/S0301-9268\(96\)00011-3](https://doi.org/10.1016/S0301-9268(96)00011-3)
- Hu, B., Xu, Y., Wan, B., Wu, X., & Yi, G. (2018). Hydrothermally altered mineral mapping using synthetic application of Sentinel-2A MSI, ASTER and Hyperion data in the Duolong area, Tibetan Plateau, China. *Ore Geology Reviews*, 101, 384–397. <https://doi.org/10.1016/j.oregeorev.2018.07.017>
- Ibrahim, U., & Mutua, F. (2014). Lineament extraction using Landsat 8 (OLI) in Gedo, Somalia. *International Journal of Science and Research*, 3(9).
- Ibrahima, E., Barnabéa, P., Ramanaidoub, E., & Pirarda, E. (2018). Mapping mineral chemistry of a lateritic outcrop in New Caledonia through generalized regression using Sentinel-2 and field reflectance spectra. *International Journal of Applied Earth Observation and Geoinformation*, 73, 653–665. <https://doi.org/10.1016/j.jag.2018.08.004>

- Ilboudo, A., Sawadogo, S., Soulama, S., Hien, E., & Prosper, Z. (2020). Spatial dynamics and risks analysis of lowlands degradation potential around of Nakanbé-Dem sub-watershed in Center-Nord of Burkina Faso (West Africa): Through multi-date study and satellite tele analysis. *European Scientific Journal*, *16*(33), 122. <https://doi.org/10.19044/esj.2020.v16n33p122>
- Ilboudo, H., Lompo, M., Wennenga, U., Napon, S., Naba, S., & Ngom, P. M. (2017). Evidence of a volcanogenic massive sulfide (Zn-Pb-Cu-Ag) district within the Tiébébé Birimian (Paleoproterozoic) Greenstone Belts, southern Burkina Faso (West-Africa). *Journal of African Earth Sciences*, *129*, 792–813. <https://doi.org/10.1016/j.jafrearsci.2017.01.020>
- Ilboudo, H., Traoré, A., Saga, S., Nonguierma, B., & Toubania, S. (2018). Geology and gold occurrences of the Gombélédougou Paleoproterozoic terrane, Houndé belt in Burkina Faso (West-Africa). *Journal des Sciences*, *18*(1), 1–12.
- Javhar, A., Chen, X., Bao, A., Jamshed, A., Yunus, M., Jovid, A., & Latipa, T. (2019). Comparison of multi-resolution optical Landsat-8, Sentinel-2 and radar Sentinel-1 data for automatic lineament extraction: A case study of Alichur area, SE Pamir. *Remote Sensing*, *11*(7), 77. <https://doi.org/10.3390/rs11070778>
- Li, N., Frei, M., & Altermann, W. (2010). Textural and knowledge-based lithological classification of remote sensing data in southwestern Prieska sub-basin, Transvaal Supergroup, South Africa. *Journal of African Earth Sciences*, *60*(4), 237–246. <https://doi.org/10.1016/j.jafrearsci.2011.03.002>
- Liu, G. J., & Philippa Mason, J. P. (2009). *Essential image processing and GIS for remote sensing* (1st ed., p. 443). John Wiley & Sons, Ltd, Publication. <https://doi.org/10.1002/9781118687963.ref>
- Loughlin, W. (1991). Principal component analysis for alteration mapping. *Photogrammetric Engineering & Remote Sensing*, *57*, 1163–1169.
- Markwitz, V., Hein, K. A. A., & Miller, J. (2016). Compilation of West African mineral deposits: Spatial distribution and mineral endowment. *Precambrian Research*, *274*, 61–81. <https://doi.org/10.1016/j.precamres.2015.05.028>
- Masurel, Q., Eglinger, A., Thébaud, N., Allibone, A., André-Mayer, A.-S., McFarlane, H., et al. (2022). Paleoproterozoic gold events in the southern West African Craton: Review and synopsis. *Mineralium Deposita*, *57*(4), 513–537. <https://doi.org/10.1007/s00126-021-01052-5>
- Milesi, J. P., Ledru, P., Feybesse, J. L., Dommanget, A., & Marcoux, E. (1992). Early Proterozoic ore deposits and tectonics of the Birimian orogenic belt, West Africa. *Precambrian Research*, *58*(1–4), 305–344. [https://doi.org/10.1016/0301-9268\(92\)90123-6](https://doi.org/10.1016/0301-9268(92)90123-6)
- Moore, G. K., & Waltz, F. A. (1983). Objective procedure for lineament enhancement and extraction. *Photogrammetric Engineering & Remote Sensing*, *49*(5), 641–647. <https://pubs.usgs.gov/publication/70011366>
- Mwaniki, M. W., Moeller, M. S., & Schellmann, G. (2015). A comparison of Landsat 8 (OLI) and Landsat 7 (ETM+) in mapping geology and visualising lineaments: A case study of central region Kenya. *The International Archives of the Photogrammetry, Remote Sensing and Spatial Information Sciences*. XL-7/W3. 36th international Symposium on Remote Sensing of Environment. <https://doi.org/10.5194/isprsarchives-XL-7-W3-897-2015>
- Naba, S. (2007). *Propriétés magnétiques et caractères structuraux des granites du Burkina Faso oriental (Craton Ouest Africain, 2,2–2,0 Ga): Implications géodynamiques*. Thèse de Doctorat (p. 175). Université Toulouse. Retrieved from <https://www.theses.fr/2007TOU30328>
- Nana, M. (1992). *Orpaillage et transformations de la vie rurale l'exemple du village de bouda dans la province du Passoré. Mémoire de maîtrise* (p. 135). Université de Ouagadougou.
- Ngom, N. M. (2022). *Apport de la Télédétection au Suivi de l'Exploitation Artisanale de l'or (Orpaillage) en Afrique de l'Ouest*. Thèse de Doctorat (p. 168). Université Cheikh Anta Diop de Dakar.
- Ngom, N. M., Baratoux, D., Bolay, M., Dessertine, A., Abass Saley, A., Baratoux, L., et al. (2022). Artisanal exploitation of mineral resources: Remote sensing observations of environmental consequences, social and ethical aspects. *Surveys in Geophysics*, *44*(1), 225–247. <https://doi.org/10.1007/s10712-022-09740-1>
- Ngom, N. M., Mbaye, M., Baratoux, D., Baratoux, L., Catry, T., Dessay, N., et al. (2020). Mapping artisanal and small-scale gold mining in Senegal using Sentinel 2 data. *GeoHealth*, *4*(12). <https://doi.org/10.1029/2020GH000310>
- Ngom, N. M., Mbaye, M., Baratoux, D., Baratoux, L., Kouassi, E. A., Kouame, J. K., et al. (2022). Recent expansion of artisanal gold mining along the Bandama River (Côte d'Ivoire). *International Journal of Applied Earth Observation and Geoinformation*, *112*, 102873. <https://doi.org/10.1016/j.jag.2022.102873>
- OCHA. Burkina Faso (Bureau de la coordination des affaires humanitaires/ONU). (2022). Rapport de situation au 20 septembre 2022. Retrieved from <https://reports.unocha.org/fr/country/burkina-faso>
- Ourhzi, Z., Algouti, A., Algouti, A., & Hadach, F. (2019). Lithological mapping using Landsat 8-OLI and aster multispectral data in Imini-Ounilla district south high atlas of Marrakech. *The International Archives of the Photogrammetry, Remote Sensing and Spatial Information Sciences*, *XLII-2/W13*, 1255–1262. <https://doi.org/10.5194/isprs-archives-XLII-2-W13-1255-2019>
- Pour, A. B., & Hashim, M. (2011). Identification of hydrothermal alteration minerals for exploring of porphyry copper deposit using ASTER data, SE Iran. *Journal of Asian Earth Sciences*, *42*(6), 1309–1323. <https://doi.org/10.1016/j.jseaes.2011.07.017>
- Pour, A. B., & Hashim, M. (2015a). Structural mapping using PALSAR data in the central gold belt, Peninsular Malaysia. *Ore Geology Reviews*, *64*, 13–22. <https://doi.org/10.1016/j.oregeorev.2014.06.011>
- Pour, A. B., & Hashim, M. (2015b). Integrating PALSAR and ASTER data for mineral deposits exploration in tropical environments: A case study from Central Belt, Peninsular Malaysia. *International Journal of Image and Data Fusion*, *6*(2), 170–188. <https://doi.org/10.1080/19479832.2014.985619>
- Rajesh, H. M. (2004). Application of remote sensing and GIS in mineral resource mapping—An overview. *Journal of Mineralogical and Petrological Sciences*, *99*(3), 83–103. <https://doi.org/10.2465/jmps.99.83>
- Research Systems. (2003). *ENVI tutorials*. Edition Copyright Research Systems, Inc. Retrieved from [http://gers.uprm.edu/geol6225/pdfs/envy\\_tutorial.pdf](http://gers.uprm.edu/geol6225/pdfs/envy_tutorial.pdf)
- Rezaei, A., Hassani, H., Moarefvand, P., & Golmohammadi, A. (2020). Lithological mapping in Sangan region in northeast Iran using ASTER satellite data and image processing methods. *Geology Ecology and Landscapes*, *4*(1), 59–70. <https://doi.org/10.1080/24749508.2019.1585657>
- Richards, J. A., & Jia, X. (2006). *Remote sensing digital image analysis an introduction* (4th ed., p. 439). Springer-Verlag Berlin Heidelberg. <https://doi.org/10.1007/3-540-29711-1>
- Shawky, M. M., El-Arafy, R. A., El Zalaky, M. A., & Elarif, T. (2019). Validating (MNF) transform to determine the least inherent dimensionality of ASTER image data of some uranium localities at Central Eastern Desert, Egypt. *Journal of African Earth Sciences*, *149*, 441–450. <https://doi.org/10.1016/j.jafrearsci.2018.08.022>
- Sheikhrhimi, A., Pour, A. B., Pradhan, B., & Zoheir, B. (2019). Mapping hydrothermal alteration zones and lineaments associated with orogenic gold mineralization using ASTER data: A case study from the Sanandaj-Sirjan Zone, Iran. *Advances in Space Research*, *63*(10), 3315–3332. <https://doi.org/10.1016/j.asr.2019.01.035>
- Speranza, C. I., Akinyemi, F. O., Baratoux, D., Benveniste, J., Ceperley, N., Driouech, F., & Helmschrot, J. (2022). Enhancing the uptake of Earth observation products and services through a multi-level transdisciplinary approach. *Surveys in Geophysics*. <https://doi.org/10.1007/s10712-022-09724-1>

- Suzen, L., & Toprak, V. (1998). Filtering of satellite images in geological lineament analyses: An application to a fault zone in Central Turkey. *International Journal of Remote Sensing*, *19*(6), 1101–1114. <https://doi.org/10.1080/014311698215621>
- Wambo, J. D. T., Pour, A. B., Ganno, S., Asimow, P. D., Zoheir, B., Salles, R. D. R., et al. (2020). Identifying high potential zones of gold mineralization in a sub-tropical region using Landsat-8 and ASTER remote sensing data: A case study of the Ngoura-Colomines goldfield, eastern Cameroon. *Ore Geology Reviews*, *122*, 103530. <https://doi.org/10.1016/j.oregeorev.2020.103530>